Journal of *Marine Science and Engineering*

MDPI

Article

Delamination-Driven Nonlinear Buckling of Metal–Composite Cylindrical Shells with Different Interfacial Strengths

Chenyang Di [1], Yunsen Hu [1], Huifeng Jiao [2], Sakdirat Kaewunruen [3] and Jian Zhang [1,*]

[1] School of Mechanical Engineering, Jiangsu University of Science and Technology, Zhenjiang 212003, China; dcy0621@stu.just.edu.cn (C.D.); yunsenhu@just.edu.cn (Y.H.)
[2] State Key Laboratory of Deep-Sea Manned Vehicles, China Ship Scientific Research Center, Wuxi 214082, China; jiaohuifeng@163.com
[3] Department of Civil Engineering, School of Engineering, University of Birmingham, Birmingham B15 2TT, UK; s.kaewunruen@bham.ac.uk
* Correspondence: zhjian127@just.edu.cn

Abstract

This study delves into the delamination-driven nonlinear buckling characteristics of metal–composite cylindrical shells with different interfacial strengths. Although surface treatments are known to affect bonding performance, their specific influences on the delamination buckling behavior of metal–composite cylindrical shells remain underexplored. Accordingly, sandblasting and polishing processes were employed to the fabrication of single-lap shear specimens. The topography of the treated surface was then characterized through scanning electron microscopy, optical profilometry, and contact angle measurements. For topography characterization and performance tests, sandblasted and polished metal–composite cylindrical shells were fabricated for hydrostatic tests. A cohesive zone model was used to analyze the influences of interfacial strength on the nonlinear buckling characteristics of metal–composite cylindrical shells, and the modeling results were validated by benchmarking them with experimental results. Subsequently, a detailed parametric study was conducted to investigate the effects of cohesive zone parameters and geometric imperfection on the load-bearing capacity of the shells. The new findings reveal that among the fabricated steel specimens, the specimens subjected to 80-mesh sandblasting exhibited the highest bond strength in single-lap shear tests, with the bond strength being 2.56 times higher than that of polished specimens. Moreover, sandblasted metal–composite cylindrical shells exhibited a 55.0% higher average collapse load than that of polished metal–composite cylindrical shells.

Keywords: cylindrical shell; metal–composite structure; delamination; buckling

check for updates

Academic Editor: Vincenzo Crupi

Received: 2 June 2025
Revised: 26 June 2025
Accepted: 29 June 2025
Published: 30 June 2025

Citation: Di, C.; Hu, Y.; Jiao, H.; Kaewunruen, S.; Zhang, J. Delamination-Driven Nonlinear Buckling of Metal–Composite Cylindrical Shells with Different Interfacial Strengths. *J. Mar. Sci. Eng.* **2025**, *13*, 1279. https://doi.org/10.3390/jmse13071279

Copyright: © 2025 by the authors. Licensee MDPI, Basel, Switzerland. This article is an open access article distributed under the terms and conditions of the Creative Commons Attribution (CC BY) license (https://creativecommons.org/licenses/by/4.0/).

1. Introduction

Underwater vehicles are indispensable for exploring mineral resources, monitoring ocean ecosystems, and safeguarding coastlines and sea life. The cylindrical shell is a critical component of underwater vehicles. Advanced materials are crucial for improving the mechanical performance of cylindrical shells, significantly enhancing their load-bearing capacity and fatigue resistance [1,2]. Because of their high fatigue resistance, specific strength, and corrosion resistance, composite materials have been extensively used in the fabrication of cylindrical shells for underwater vehicles [3–6]. Metal–composite cylindrical pressure hulls combine the advantages of steel pressure hulls and composite pressure hulls, exhibiting excellent mechanical performance and being convenient to manufacture [7–9].

In summary, metal–composite cylindrical shells have garnered widespread attention from scholars as an optimal solution for underwater vehicle hulls, owing to their superior performance and manufacturability. A disadvantage of cylindrical shells is that they typically fail through buckling in deep-sea environments, with their buckling load determined by their geometry imperfections and material properties [10–13].

Thus, understanding and improving the buckling resistance of cylindrical shells remains a central concern in deep-sea structural design. Many studies have investigated the buckling characteristics of metal–composite cylindrical shells. Zuo et al. [7–9] found that fully or helically wrapping composite on metal liner can enhance the load-bearing capacity of a metal cylinder. They demonstrated that metal–composite cylindrical shells have excellent structural efficiency and are convenient to manufacture. Wang et al. [14] investigated the effects of geometric parameters on the buckling load of aluminum–composite cylindrical shells, using both experimental and numerical methods. Cai et al. [15] developed a methodology based on reliability principles for designing the load and resistance factor of subsea composite pressure vessels, and they validated their results through experimental testing. Li [16] proposed a collaborative approximation methodology for designing aluminum–composite cylindrical shells, with the goal of minimizing weight. Sumana et al. [17] explored the effect of wrapping angles on the buckling characteristics of aluminum–composite cylindrical shells. They found that a wrapping angle combination of $0^\circ/90^\circ$ had the strongest influence on buckling characteristics. These works highlight the importance of geometric design and composite wrapping strategies in improving the structural efficiency of hybrid cylindrical shells. In addition to these studies, Rezaiee-Pajand et al. [18] developed a mixed interpolated formulation for nonlinear analysis of functionally graded sandwich plates and shells, using equivalent single layer theory and triangular shell elements to effectively address large displacements, finite rotations, and locking effects. Furthermore, Ghandehari et al. [19] investigated the multiscale vibrational behavior of nested dual conical shells reinforced with temperature-sensitive nanomaterials, revealing the significant influence of thermal conditions, boundary stiffness, and nanofiller orientation on their dynamic responses. These studies provide valuable modeling insights that support the numerical analysis of composite cylindrical shells under complex loading environments.

Research on the causes of delamination-driven buckling in composite cylindrical shells has focused on two main mechanisms: adhesive failure and initial delamination [20]. Kachanov [21,22] investigated the delamination buckling of glass-fiber-reinforced composite pipes. He proposed that when external pressure exceeds a critical threshold, the inner thin layer of these pipes suddenly delaminates, causing delamination buckling. Rasheed and Tassoulas [23] conducted finite element analysis of plane-strain problems related to the delamination propagation in pipes under external pressures. Their results confirmed that before complete failure, delamination of the inner thin layer causes delamination buckling. Fu and Yang [24] analyzed delamination propagation in composite cylindrical shells under external pressure by using laminate theory and the Griffith criterion, exploring the effects of initial debonding size and position on delamination propagation. Wei et al. [25] examined the effects of initial delamination shape and depth on buckling characteristics. Their results suggested that buckling of a composite cylindrical shell causes delamination propagation and that buckling load is significantly influenced by the axial initial delamination. These findings highlight the importance of interfacial defects and delamination parameters in governing the buckling of composite cylindrical shells. Moreover, they used the adhesive failure model to analyze the interlayer adhesive failure of deep-sea sandwich pipelines, composite material reinforcement, and metal structure repair. Qu et al. [26] conducted reliability analysis of the failure strength of metal–polypropylene deep-sea sandwich pipes,

using the cohesive element to simulate the epoxy resin adhesive bonding between metal and polypropylene. Their failure criterion was based on quadratic stress criterion, with the failure evolution following a power law. Wan et al. [27,28] performed plane-strain finite element analysis of the pressure capacity of deep-sea sandwich pipes. The bonding parameters between the metal pipes and the core layer were obtained through tests on sandwich pipe specimens. An empirical equation was then formulated to estimate the pressure capacity on the basis of geometric and material parameters. Teng et al. [29–32] proposed using composite materials to strengthen or repair metal structures. They systematically investigated the interfacial mechanical properties and bonding failure between metals and composites. These efforts emphasize the necessity of accurate modeling and empirical prediction of interfacial failure in hybrid cylindrical shells.

Surface quality reflects the overall condition of a material's surface and is typically characterized by parameters such as surface energy, chemical composition, surface roughness, and topography. Surface treatments, including mechanical, electrochemical, laser, and resin precoating treatments, significantly enhance bond strength by modifying surface characteristics. Mechanical treatment methods promote mechanical interlocking through surface roughening, which increases bond strength by providing more surface area for adhesive contact and enhancing the adhesion between the material and adhesive. Bond strength is a crucial mechanical property that reflects the internal cohesion of materials, with its physical basis rooted in intermolecular forces. Budhe et al. [33] emphasized that the adhesive bond strength of joints are significantly influenced by the surface roughness of the joints. Zielecki et al. [34] proposed that the shear strength of adhesive joints is primarily influenced by the effective surface area, and can be enhanced by mechanical treatments such as grit blasting. Chemical and electrochemical treatments (such as etching or anodization) produce porous structures that enhance bond strength. Kadlečková et al. [35] noted that duralumin with a porous structure created using an appropriate etchant combination had a 9.9% higher lap shear strength than did sandblasted specimens. Ye et al. [36] proposed that using a fluoride electrolyte to construct a nanotube array on titanium can enhance bond strength. Laser and plasma treatments improve adhesion by removing contaminants and creating micropatterns. Maressa et al. [37] used laser treatment to create microtextures on titanium alloy surfaces, thereby increasing bond strength by 30%. Schweizer et al. [38] employed short-pulse infrared lasers on composites, enhancing bond strength by 140%. Saleema et al. [39] treated aluminum alloys with helium–oxygen plasma, achieving a high shear strength (24 MPa) and demonstrating the potential of this plasma to modify aluminum alloys. Resin pre-coatings enhance interfacial bonding by penetrating and filling microcavities, a process similar to improved wettability. This allows the adhesive to spread more evenly across the surface, thereby increasing the contact area at the bonding interface. Wang et al. [40] developed a resin precoating technology that increased the strength of sandblasted steel joints by 46.9%, an increase that was attributable to the resin filling micropores. Hu et al. [41,42] showed that resin precoating combined with acid pickling, sanding, and other pretreatments considerably increased the strength of metal–composite bonds. These treatments demonstrate considerable potential for improving interfacial strength in bonded structures.

From the review of the previous studies, there have been few studies on delamination buckling caused by adhesive failure, as well as the effect of steel surface quality on steel-composite bonding performance. Choqueuse et al. [43] conducted hydrostatic tests on five steel–composite cylindrical hulls, but observed inconsistent test results and premature delamination buckling, due to inadequate interfacial quality control. Zuo et al. also observed delamination in hydrostatic tests of a steel–composite cylindrical pressure hull [7]. Based on this structure, Zhang et al. investigated the buckling behavior of a steel–composite

cylindrical pressure hull with initial delamination, using numerical and experimental methods. Two practical equations were proposed for predicting linear and nonlinear buckling loads based on delamination parameters [44]. Although surface treatment techniques have demonstrated potential for enhancing interfacial bonding strength and delaying delamination initiation in composite structures, their application in pressure hull systems remains unexplored. The relationship between interface reinforcement and buckling load enhancement in pressure hull applications therefore requires systematic investigation.

Previous studies primarily focused on adhesive failure and initial delamination as the main causes of delamination buckling. However, they did not systematically investigate the effect of surface treatments on interfacial strength and how it affects the buckling characteristics of metal–composite cylindrical shells. While surface treatment techniques have been widely applied to enhance the bonding performance of composite structures, their roles in improving the load-bearing capacity and delaying delamination initiation in cylindrical shells have not been thoroughly examined. By employing sandblasting and polishing treatments to modify surface roughness and wettability, this research provides new insights into the influence of interfacial quality on the delamination buckling of metal–composite cylindrical shells.

The rest of this paper is outlined as follows. Section 2 describes the manufacturing processes of single-lap shear specimens and metal–composite cylinders, including surface treatment of metal layers and bonding with composite layers using an epoxy adhesive, along with the experimental methodology. Section 3 elucidates the bonding performance of sandblasted and polished single-lap shear specimens, establishing a theoretical basis for analyses of the delamination buckling of metal–composite cylinders. Section 4 provides the main conclusions. This study contributes a novel understanding of delamination buckling and improves the buckling resistance of cylindrical shells, thereby offering guidance for the reliable application of metal–composite cylindrical shells in deep-sea environments.

2. Materials and Methods

Advanced surface characterization techniques were employed to analyze the surface topography of sandblasted and polished metal surfaces. To identify optimal sandblasting conditions, single-lap shear specimens were fabricated, and their bond strength was tested. Sandblasted and polished metal–composite cylindrical shells were fabricated on the basis of the single-lap shear test results, and their fabrication accuracy and delamination buckling characteristics were evaluated under external pressure.

2.1. Surface Quality and Bond Strength Testing

The topography of sandblasted and polished metal surfaces was measured using a field-emission scanning electron microscope (ZEISS Gemini SEM 360, Carl Zeiss AG, Oberkochen, Baden-Württemberg, Germany). The sandblasted specimens were scanned under a working distance of 0.72 cm and an accelerating voltage of 3000 V. The scanning results were captured at a magnification of 200× (Figure 1).

Three-dimensional (3D) surface roughness was measured using a VK-X3000 3D surface profiler (Keyence Corporation, Itasca, IL, USA) in laser confocal scanning mode. The laser wavelength, maximum measurement frequency, and maximum laser output of the measurement head were 661 nm, 125 Hz, and 1.0 mW, respectively. Measurements were conducted on a 1061 × 1415 μm^2 area of each sandblasted specimen. The measurement data were imported into the software program EXScan HX (version 1.4.1.2) of the 3D profiler for analysis, to determine the roughness parameters. The surface-roughness measurement parameters conformed to the ISO 25178 standard [45]. The measured surface height profiles are displayed in Figure 2. The measured roughness parameters are presented in Table 1.

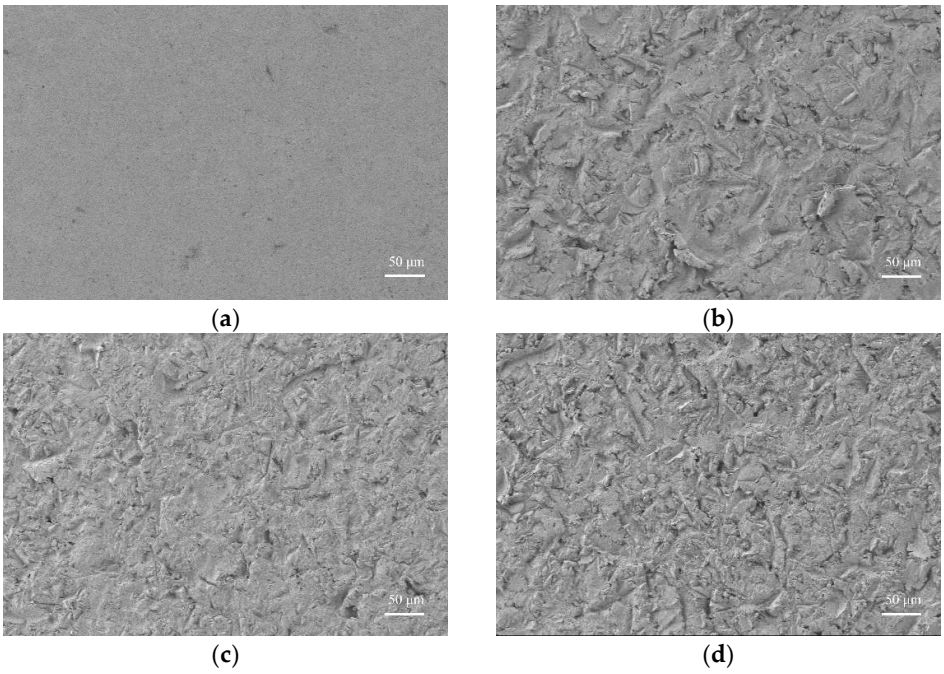


Figure 1. Scanning electron micrography images of stainless steel surfaces: (**a**) as-received polished specimen and specimens sandblasted with (**b**) 80-mesh, (**c**) 180-mesh, and (**d**) 320-mesh corundum.

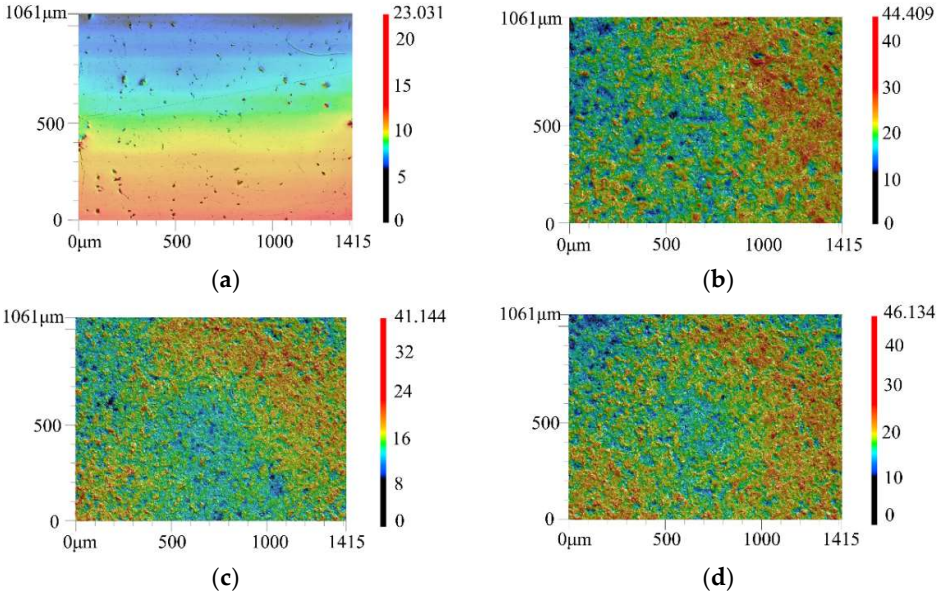


Figure 2. Surface height profiles on the steel surface: (**a**) as-received polished specimen and specimens sandblasted with (**b**) 80-mesh, (**c**) 180-mesh, and (**d**) 320-mesh corundum.

Table 1. Surface-roughness parameters of steel specimens subjected to sandblasting with different grit sizes.

Mesh	R_a	R_q	R_t	R_p	R_v
			μm		
0	0.147	0.283	4.631	3.562	1.069
80	2.448	3.084	19.183	9.704	9.467
180	1.815	2.363	16.999	8.388	8.610
320	1.941	2.489	17.112	8.644	8.425

Note: R_a is arithmetic mean roughness; R_q is root mean square roughness; R_t is total height of the profile; R_p is maximum profile peak height; R_v is maximum profile valley depth.

The contact angles between the steel surface and liquids were measured using the sessile drop method and an OCA15EC system (DataPhysics Instruments GmbH, Nürtingen, Baden-Württemberg, Germany). A 2 μL droplet of distilled water was applied to the surface of each sandblasted specimen, and contact angles were analyzed using software OneAttension, version 3.2 (Nanoscience Instruments, Phoenix, AZ, USA). Contact angles are displayed in Figure 3.

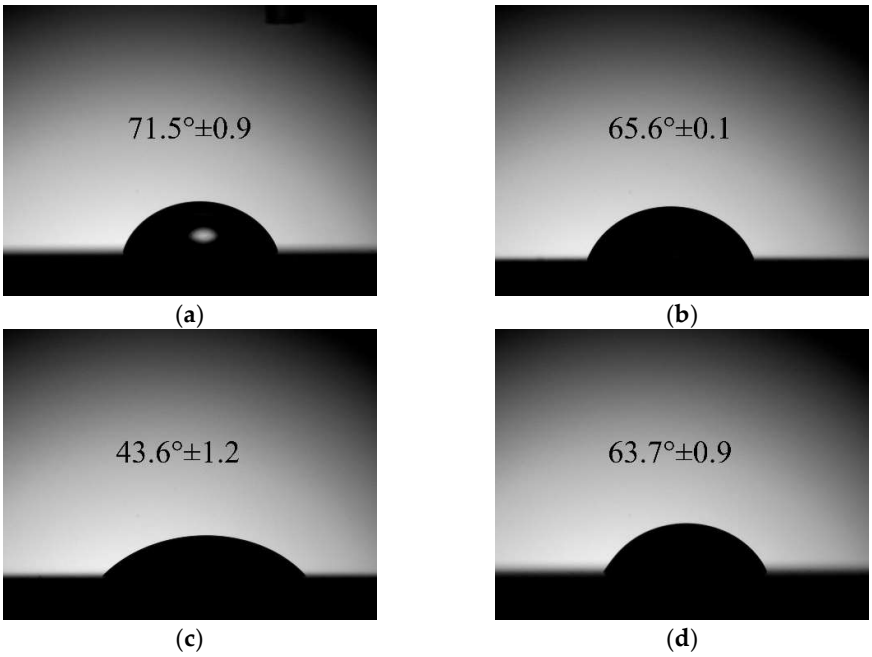


Figure 3. Contact angles of water on steel surfaces: (**a**) as-received polished specimen and specimens sandblasted with (**b**) 80-mesh, (**c**) 180-mesh, and (**d**) 320-mesh corundum.

The bond strength between two steel pieces under different sandblasting conditions was tested using an MZ-5001D1 universal testing machine (Jiangsu Mingzhu Testing Machinery, Yangzhou, China). The bond strength testing process conformed to the ASTM D5868 standard (2014). The quasi-static shear tests of single-lap joints were conducted on this machine, where the crosshead displacement rate was controlled at 1 mm/min during the entire loading phase. Six tests were performed for each type of specimen, and the corresponding average bond strengths were determined. The bond strengths of specimens are presented in Table 2 and Figure 4.

Table 2. Bond strengths of various types of sandblasted steel specimens in single-lap shear tests.

Mesh	Sample-1	Sample-2	Sample-3	Sample-4	Sample-5	Sample-6	Mean
	MPa						
0	6.52	4.52	6.98	7.40	5.32	7.83	6.43
80	22.25	22.63	22.79	22.80	23.05	23.61	22.86
180	20.70	20.95	21.69	22.08	22.12	22.30	21.64
320	17.90	18.06	18.09	18.27	20.34	21.63	19.05

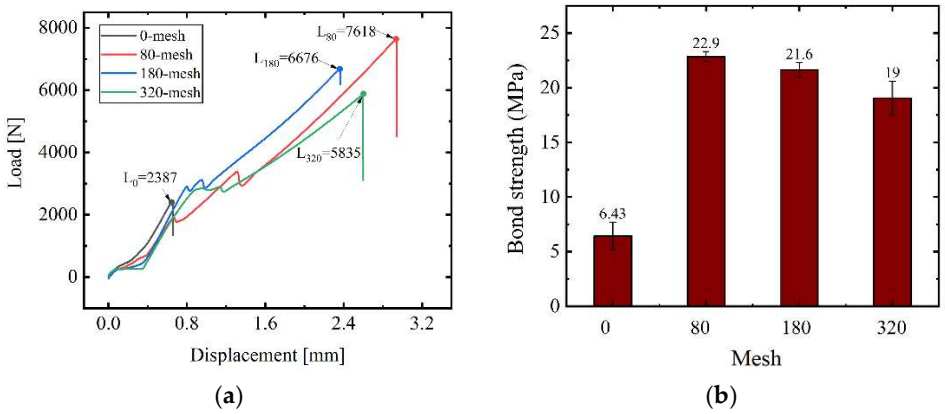


Figure 4. Results of single-lap shear tests for sandblasted steel specimens: (**a**) representative load–displacement curves and (**b**) average bond strength (error bars indicate standard deviations).

2.2. Fabrication of Single-Lap Shear Specimens

Single-lap shear specimens were fabricated in accordance with the ASTM D5868 standard [46]. The geometric dimensions of these specimens are depicted in Figure 5. The specimen preparation procedure is described as follows. Commercially available steel plates were laser-cut into pieces with a length, width, and thickness of 101.6, 25.4, and 3 mm, respectively. A 25.4 × 25.4 mm^2 area at the end of each piece was designated as the overlap area. This area was treated through sandblasting by using corundum of different grit sizes, including 0 (surface polishing), 80, 180, and 320 mesh. Following this surface treatment, HG302-A resin (Jiangsu Boshi Carbon Fiber Technology, Nanjing, China) was applied to the overlap region. Medium-sized binder clips were then placed on the outer edges of the bonding regions of two pieces to maintain adequate compressive pressure. Square pieces with a side length of 3 mm were bonded to the non-sandblasted end of the pieces by using the same bonding method. The specimens were initially cured at room temperature (15–23 °C) for 6 h to achieve the desired thickness, following which they were completely cured in an oven at 120 °C and then held at this temperature for 90 min. Finally, any excess resin was carefully removed to prevent it from affecting the bond strength.

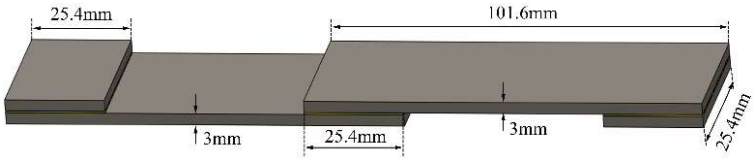


Figure 5. Schematic of specimen fabricated in accordance with the ASTM D5868 standard for use in a single-lap shear test.

2.3. Fabrication of Cylindrical Shells

Figure 6a and Table 3 depicts the geometric dimensions of the sandblasted and polished metal–composite cylinders. These cylinders possessed identical geometric parameters, with their effective length (L), nominal steel layer thickness (t_{s-non}), nominal composite layer thickness (t_{c-non}), and outer metal cylinder radius (R) being 150, 1.2, 1.2, and 70 mm, respectively. Metal–composite cylinders were either sandblasted or polished, to achieve different surface properties (Figures 6b and 7c).

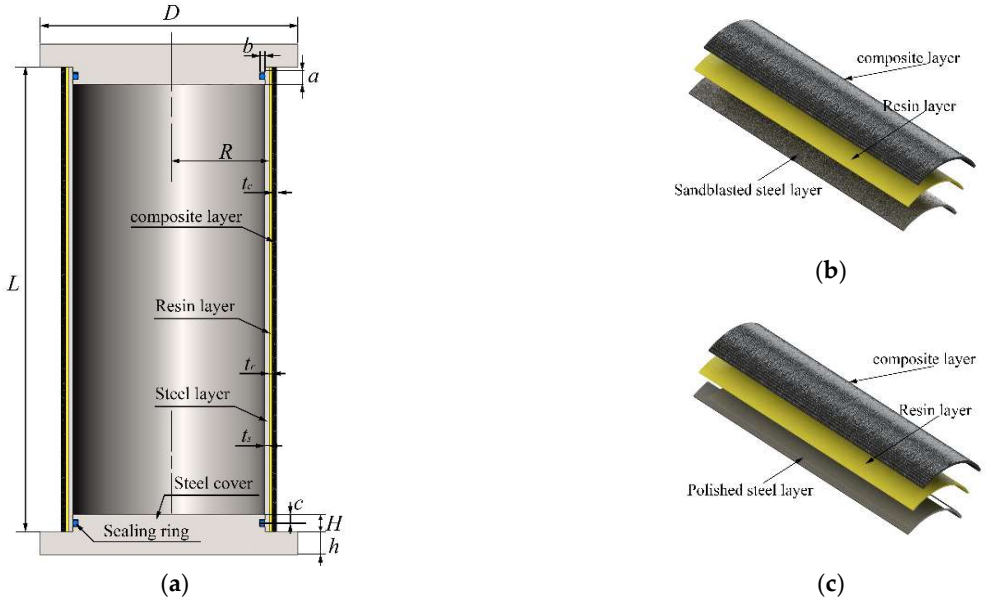


Figure 6. Schematic of polished and sandblasted metal–composite cylindrical shells: (**a**) cross-sectional view of polished and sandblasted hulls, (**b**) partial view of a polished metal–composite hulls, and (**c**) partial view of a sandblasted metal–composite cylindrical shells.

Table 3. Geometric parameters of sandblasted and polished metal–composite cylinders.

Sample	*L*	*R*	$t_{s\text{-}nom}$	$t_{c\text{-}nom}$	*D*	*a*	*b*	*c*	*h*	*H*
	mm									
cylinder	162	70	1.2	1.2	90	4.25	2	3	8	6

Note: *L* is length; *R* is radius; $t_{s\text{-}non}$ is nominal thickness of steel layer; $t_{c\text{-}nom}$ is nominal thickness of composite layer; *D* is diameter of bottom flange; *a* is width of groove; *b* is depth of groove; *c* is distance between groove and top flange; *h* is height of bottom flange; *H* is height of top flange.

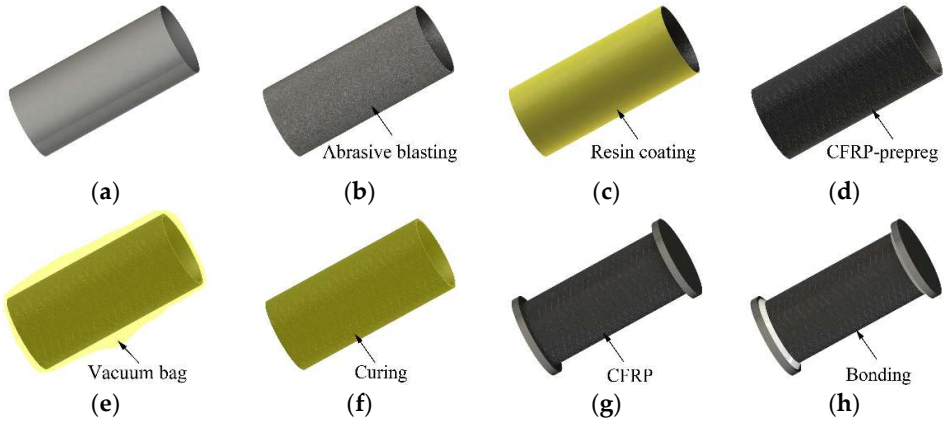


Figure 7. Fabrication process for sandblasted metal–composite cylinders: (**a**) steel cylinder, (**b**) abrasive blasting and cleaning, (**c**) resin coating, (**d**) CFRP prepreg wrapping, (**e**) vacuum bag wrapping, (**f**) vacuuming and hybrid cylinder curing, (**g**) hybrid cylinder assembly process, and (**h**) sealing and bonding.

The aforementioned cylinders were fabricated using a vacuum bagging technique (Figure 7). First, steel cylinders were cut to the required length by using wire electrical-discharge machining technology (Figure 7a). The surfaces of these cylinders were then sandblasted or polished under the optimal grit size (Figure 7b) obtained in the single-lap shear tests (Section 2.2). Subsequently, alcohol and acetone were used to remove

contaminants from the steel cylinder surfaces. After contaminant removal, HG302-A resin was uniformly applied over the steel cylinder surfaces (Figure 7c). Next, T300 carbon-fiber-reinforced polymer (CFRP) prepreg (Weihai Zimingda New Materials Technology, Weihai, Shandong, China) was laid on the cylinder surfaces (Figure 7d). Each cylinder was then wrapped with a vacuum bagging film and placed in a hot-press chamber for continuous vacuuming (Figure 7e). The temperature inside the chamber was increased to 120 °C, and the chamber was maintained at this temperature for 90 min (Figure 7f). This vacuum bagging technique enabled the effective removal of surplus resin and air during the curing process [47,48]. Thus, imperfections in the composite layers were reduced, ensuring consistent material performance [49]. Sealing rings were placed into the grooves of steel covers mounted at both ends of each metal–composite cylinder (Figure 7g). Finally, the joints between each cylinder and cover were sealed with Araldite 2015 epoxy resin (Figure 7h).

2.4. Fabrication Accuracy and Hydrostatic Testing

The wall thicknesses of the fabricated cylinders were measured to evaluate fabrication accuracy and develop a numerical model of the fabricated cylinders. Before conducting thickness measurements, an ultrasonic device (PX-7, Dakota Ultrasonics, Scotts Valley, CA, USA) and a customized micrometer were calibrated using standard blocks with known thicknesses. The wall thickness measurement complied with the ISO 16809 standards [50]. As displayed in Figure 8a, the ultrasonic device was used to measure the wall thicknesses of the fabricated steel cylinders. The thickness was measured at 192 points on the external surface of each steel cylinder, with 16 points being uniformly distributed at intervals of 10 mm and 12 points being uniformly distributed at intervals of 30°, along the axial and circumferential directions, respectively. The thickness measurement results for the steel cylinders are summarized in Table 4. An ultrasonic device is unsuitable for measuring the thickness of nonhomogeneous materials; therefore, the customized micrometer was employed to determine the thicknesses of the fabricated metal–composite cylinders. The number and distribution of thickness measurement points on the metal–composite cylinders were the same as those on the steel cylinders (Figure 8b). Table 5 presents the detailed thickness measurement results for the metal–composite cylinders.

To accurately assess the geometric fabrication accuracy of the sandblasted and polished metal–composite cylinders, a 3D optical scanner, EinScan HX (Shining 3D Technology Company Limited, Hangzhou, China) was used to conduct laser scanning of the external surface of each cylinder. As depicted in Figure 8c, many circles markers were randomly placed on the surface of each cylinder as spatial reference points to assist the combination of the geometric data. After scanning was conducted from multiple angles, a precise digital model of the cylinder geometry was generated using in-house software EXScan HX (version 1.4.1.2) for subsequent analysis. The geometric deviations between the scanned and ideal models are illustrated in Figure 9.

Hydrostatic tests were performed on metal–composite cylinders (Figure 8d) in a hydrostatic chamber. The pressure was monitored using a sensor (Hangzhou Meiyi Automation Technology, Hangzhou, China) located at the top of the chamber, and pressure data were collected using a dynamic acquisition system (DH5902N, Jiangsu Donghua Calibration and Testing, Taizhou, China) at a frequency of 50 Hz. The pressure in the chamber was gradually increased, using a manual pump, until a sharp explosion sound was heard. The pressure curves and post-buckling modes of the fabricated metal–composite cylinders are displayed in Figures 10 and 11, respectively. The collapse pressures of these cylinders are presented in Table 5.

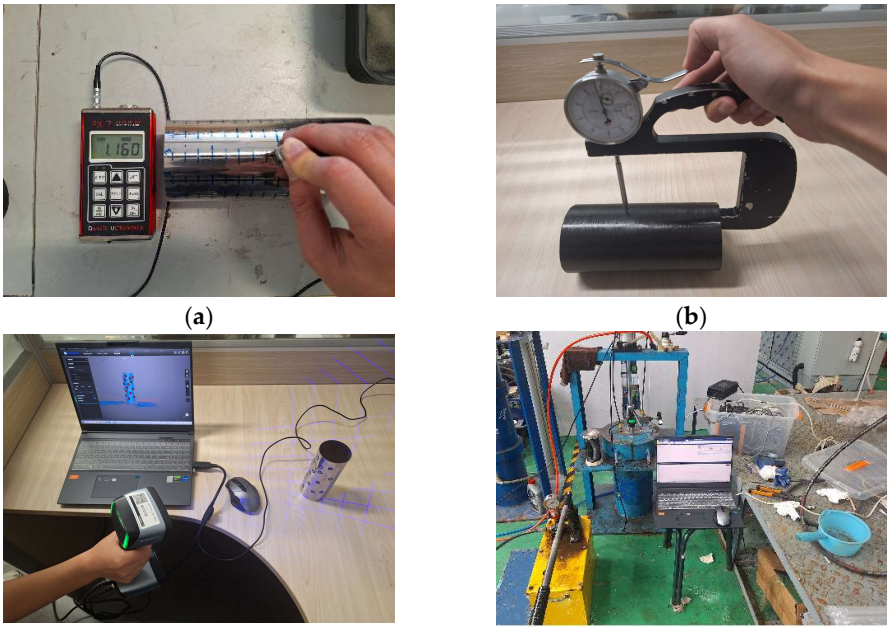


Figure 8. Measurement and testing setups for the fabricated specimens: (**a**) measurement of the steel layer thickness of the fabricated shell, (**b**) measurement of the overall thickness of the fabricated shell, (**c**) measurement of the shape of the fabricated shell, and (**d**) hydrostatic testing of the fabricated shell.

Table 4. Wall thicknesses of the steel layer in the fabricated sandblasted and polished metal–composite cylinders.

Sample	$t_{s\text{-}av}$	$t_{s\text{-}max}$	$t_{s\text{-}min}$	$t_{St.\ dev.}$
	mm			
Sandblasted cylinder-1	1.137	1.230	1.074	0.027
Sandblasted cylinder-2	1.140	1.176	1.114	0.015
Polished cylinder-1	1.149	1.434	1.122	0.051
Polished cylinder-2	1.137	1.206	1.098	0.029

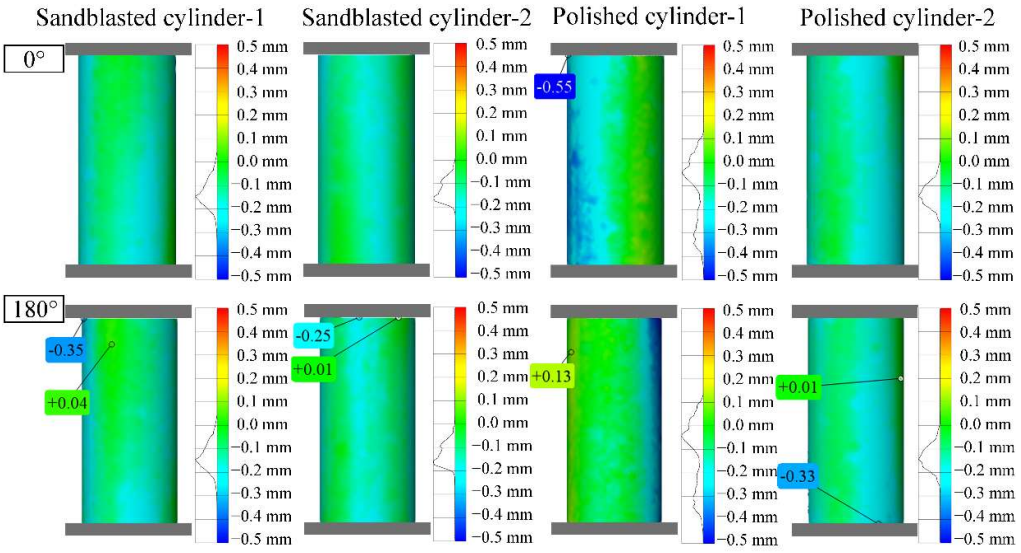


Figure 9. Geometric deviations of the fabricated sandblasted and polished metal–composite cylinders.

Table 5. Geometric properties and collapse load of the fabricated sandblasted and polished metal–composite cylinders.

Sample	$t_{s\text{-}av}$	$t_{s\text{-}max}$	$t_{s\text{-}min}$	$t_{St.\ dev.}$	P_{test}	Mean
	mm				MPa	
Sandblasted cylinder-1	2.378	2.467	2.340	0.043	21.929	22.093
Sandblasted cylinder-2	2.390	2.492	2.300	0.059	22.257	
Polished cylinder-1	2.391	2.462	2.360	0.035	15.444	14.258
Polished cylinder-2	2.415	2.605	2.340	0.089	13.072	

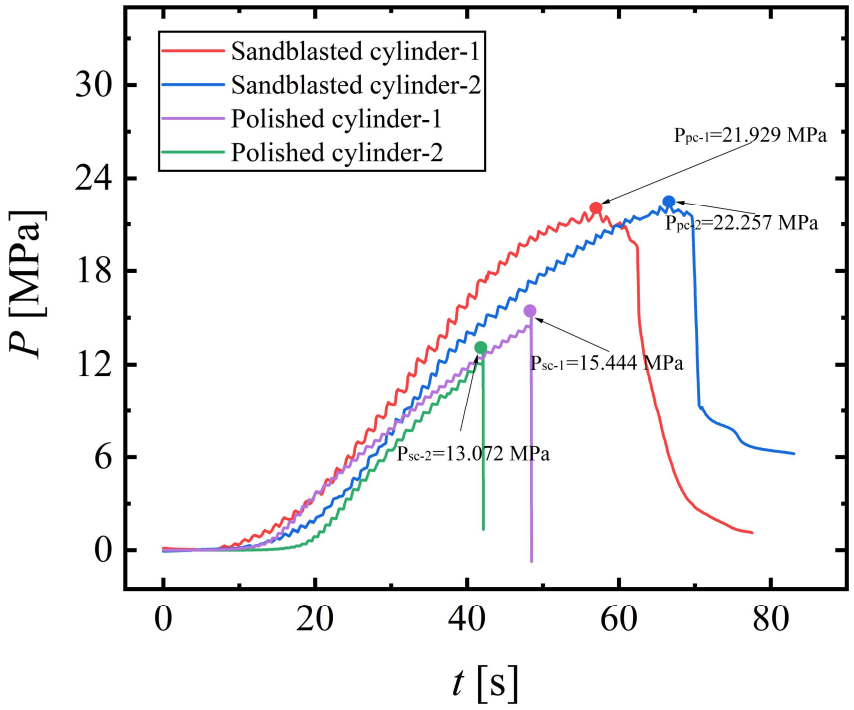


Figure 10. Hydrostatic pressure of the fabricated sandblasted and polished metal–composite cylinders.

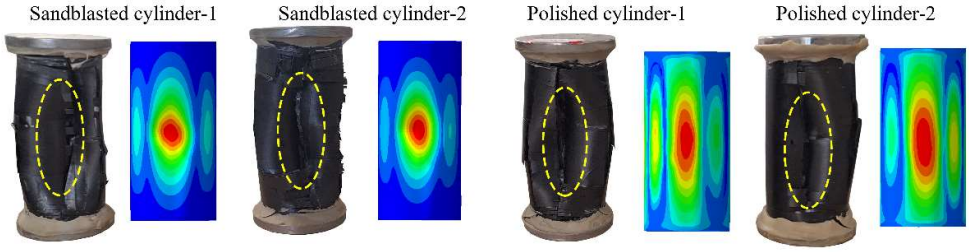


Figure 11. Images of the fabricated sandblasted and polished metal–composite cylinders after their buckling in hydrostatic testing and corresponding numerical post-buckling modes.

3. Results and Discussion

The influence of surface quality on the bond strength of the fabricated single-lap shear specimens was investigated, thus obtaining crucial information for the selection of the manufacturing parameters of metal–composite cylinders. Subsequently, the numerical and experimental results obtained for the sandblasted and polished metal–composite cylinders were compared. Finally, the effects of cohesive zone parameters and imperfection sensitivity on the buckling load of these cylinders were analyzed using the Riks method, which is generally employed to predict the unstable, geometrically nonlinear collapse of a structure.

3.1. Experimental Investigations

3.1.1. Micro-Structural Properties of Bonding Interfaces Between the Steel and Composite

Scanning electron microscopy (SEM) images indicated a clear relationship between the grit size of corundum and the surface topography of the fabricated steel specimens. As displayed in Figure 1a, the polished (0 mesh) steel surface exhibited an extremely smooth topography. By contrast, a large number of pits and peaks were randomly distributed on the sandblasted steel surfaces (Figure 1b–d). This topographical feature is typical of steel specimens subjected to sandblasting treatment [51,52]. The grit size in sandblasting had a minimal effect on the produced topographic features, but considerably influenced the number of pits and peaks. Specifically, this number increased with a decrease in grit size.

The surface topographies observed in the height profiles of the specimens were consistent with those observed in the SEM images. As depicted in Figure 2a, although the polished specimens exhibited a smooth topography, they contained small defects, which were likely caused by compression and impact during transportation. As presented in Table 1, the polished specimens had the lowest roughness among all fabricated steel specimens (R_a = 0.147 μm). This low roughness was attributable to the use of corundum with extremely fine grits during polishing. The roughness parameters of the sandblasted specimens were notably higher than were those of the polished specimens. Among all specimens, the 80-mesh sandblasted specimen exhibited the highest roughness (R_a = 2.448 μm), which was likely attributable to the use of coarse-grit corundum with high kinetic energy in the sandblasting process for this specimen. Such corundum created large and deep pits during the sandblasting process, leading to a high surface roughness. However, the roughness of the 180-mesh sandblasted specimen (R_a = 1.815 μm) was lower than that of the 320-mesh sandblasted specimen (R_a = 1.941 μm). This result was possibly due to the surface of the 320-mesh sandblasted specimen failing to achieve a morphological steady state under a short sandblasting duration [53].

The polished and sandblasted specimens exhibited good surface wetting. As presented in Figure 3, the polished specimens exhibited the highest contact angle (71.5°) and thus the lowest wettability among the specimens. The contact angles of the 80-, 180-, and 320-mesh sandblasted specimens were 65.6°, 43.6°, and 63.7°, respectively. These results indicate that the sandblasted specimens exhibited good wetting, which allowed the steel surface to maintain stable bonding performance with the adhesive. Because the same sandblasting process was applied in all cases, any influence from compositional variations was excluded. The reductions in contact angles were likely caused by increased surface roughness, with wettability generally improving as the roughness decreased. The observed results were consistent with the principles of the Wenzel model [54], which states that increased roughness enhances wettability for hydrophilic surfaces.

The bond strengths of the sandblasted specimens in the single-lap shear tests were considerably higher than were those of the polished specimens. As displayed in Figure 4a, before fracture, the polished specimens exhibited quasilinear tensile behavior, whereas the sandblasted specimens showed distinctly nonlinear tensile behavior. The nonlinear response was marked by a sudden drop in force, which was caused by the slip between the specimens and fixture components. After the maximum load was reached, adhesive failure occurred at the metal–adhesive interface in all specimens. The bond strength was determined by dividing the maximum load by the bonding area. The average bond strengths of the specimens subjected to polishing, 80-mesh sandblasting, 180-mesh sandblasting, and 320-mesh sandblasting were 6.43, 29.3, 27.6, and 25.4 MPa, respectively. The 80-mesh sandblasted specimens had a 256% higher bond strength than did the polishing specimens. This improvement was attributable to the enhanced surface roughness caused by sandblasting, which increased the effective bonding area and strengthened mechanical interlocking [55].

Therefore, 80-mesh corundum sandblasting treatment is highly recommended for adhesively bonded metal–composite cylinders.

3.1.2. Measured Geometric Properties of the Fabricated Metal–Composite Cylinders

The thickness measurements for the fabricated cylinders demonstrated high repetitiveness and reasonable precision. As presented in Table 4, the average thicknesses of two sandblasted steel cylinders (1.137 and 1.140 mm) were similar to those of two polished steel cylinders (1.137 and 1.149 mm). These results indicate that the treatment method (polishing or sandblasting) had a negligible influence on cylinder thickness, which enabled an equivalent comparison between the fabricated sandblasted and polished metal–composite cylinders. The standard deviations of the thicknesses of four steel cylinders ranged from 0.015 to 0.051, further confirming the high repetitiveness and reasonable precision of the manufacturing process. The average thicknesses of the fabricated sandblasted and polished metal–composite cylinders ranged from 2.378 to 2.415 mm, closely aligning with the nominal wall thickness of 2.4 mm. The standard deviations of the thicknesses of the fabricated metal–composite cylinders (0.035–0.089) were higher than those of the steel cylinders (0.015–0.051). This result was attributable to defects, such as voids, resin-rich regions, and fiber wrinkling, introduced during the manual layup process for the metal–composite cylinders [56]. In contrast to these cylinders, the steel cylinders were produced through an automated manufacturing process.

The geometric deviations of the fabricated cylinders were mainly caused by deformations resulting from cold pressing and laser cutting. As shown in Figure 9, the deviations presented as axial bulges and dents, which are typical geometric imperfections resulting from the cold-rolling process, and have been commonly reported in studies on the buckling characteristics of steel cylinders [7,8,57,58]. The lower and upper deviations of the fabricated cylinders ranged from -0.25 to -0.55 mm and from 0.01 to 0.13 mm, respectively. Notably, most of these deviations were concentrated at the ends of the cylinders, and were attributable to the deformation caused by laser cutting. The aforementioned findings highlight the fact that the cold-pressing and laser-cutting techniques introduced minor geometric imperfections into the fabricated cylinders, and that these imperfections did not notably affect the overall dimensional accuracy of the cylinders.

3.1.3. Mechanical Properties of the Fabricated Metal–Composite Cylinders

Surface quality considerably influenced the pressure histories of the fabricated metal–composite cylinders. As displayed in Figure 10, the pressure initially increased and then transitioned to nonlinear regions and sharply decreased. To maintain quasistatic conditions, the loading rates for the sandblasted and polished metal–composite cylinders were controlled to approximately 0.35 MPa/s. The stepwise increase in each pressure curve was attributable to the manual operation of the water pump during the hydrostatic tests. The average collapse loads of the sandblasted and polished metal–composite cylinders were 22.093 and 14.258 MPa, respectively. Thus, the collapse load of the sandblasted metal–composite cylinders was 55.0% higher than was that of the polished metal–composite cylinders. This difference in collapse load was related to variations in interfacial strength. Sandblasting increased surface roughness, thus enhancing the bond strength and structural strength of the metal–composite interface, which contributed to a higher collapse load.

The collapse modes of the fabricated sandblasted and polished metal–composite cylinders exhibited local concavities, which are characteristic of the collapse behavior of shells of revolution [58–62]. The locations of these concavities were influenced by the initial stochastic geometric imperfections. Axial fracturing was observed in the composite layer of each sandblasted and polished metal–composite cylinder, as displayed in Figure 11.

Although surface quality did not influence the collapse modes of these cylinders, it affected the extent of delamination exhibited by the cylinders. Specifically, large delaminations and polished surfaces were observed through cracks in the polished metal–composite cylinders, whereas almost no sandblasted surface was observed through cracks in the sandblasted metal–composite cylinders. This difference was attributable to the surface quality of the sandblasted metal–composite cylinders being higher than that of the polished metal–composite cylinders. This enhanced surface quality increased the bond strength between the steel and composite layers, thereby reducing the likelihood and extent of delamination.

3.2. Numerical Investigations

3.2.1. Cohesive Zone Model

To predict the interfacial damage behaviors of metal–composite cylinders with different surface properties, a cohesive zone method was used for numerical analysis. This approach effectively simulates the initiation and growth of delamination at interfaces, enabling the damage analysis without the definition of initial cracks [63]. The bilinear mixed-mode response of cohesive elements is illustrated in Figure 12.

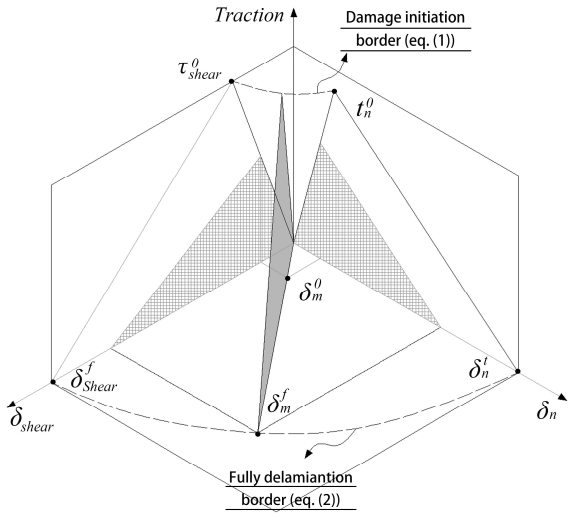


Figure 12. Illustration of the bilinear traction–separation law in cohesive elements.

In mixed-mode damage, the maximum nominal stress criterion [Equation (1)] is used to assess the initiation of damage.

$$max\left\{\frac{\langle t_n\rangle}{t_n^0}, \frac{t_s}{t_s^0}, \frac{t_t}{t_t^0}\right\} = 1 \quad (1)$$

where t_n is the normal traction stress along local axis 3, t_s is the shear traction stress along local axis 2, and t_t is the shear traction stress along local axis 1. Moreover, t_n^0, t_s^0, and t_t^0 represent the peak nominal stresses corresponding to deformations purely normal to the interface (mode I), deformations purely in the first shear direction (mode II), and deformations purely in the second shear direction (mode II), respectively. Notably, pure compressive deformation or stress does not lead to the initiation of damage [64,65].

The evolution of structural damage is determined by the energy dissipated during failure. During the delamination propagation stage, the fracture energy can be expressed as a function of the mode mix, governed by a power law criterion. As indicated by Equation (2), G_n^C, G_s^C, and G_t^C must be specified, with these parameters representing the fracture energies necessary to initiate failure in the normal, first-shear, and second-shear directions, respectively. The exponent α governs the degree of interaction between different

fracture modes. In this study, α is taken as 1. Equation (2) is used to model the fracture energy evolution during delamination propagation under mixed-mode loading.

$$\left\{\frac{G_n}{G_n^C}\right\}^{\alpha}+\left\{\frac{G_s}{G_s^C}\right\}^{\alpha}+\left\{\frac{G_t}{G_t^C}\right\}^{\alpha}=1 \tag{2}$$

Following crack initiation, the damage evolution process is quantified using the damage factor d, which monotonically increases from 0 to 1. The relationship between d and the traction stress is expressed as follows:

$$\mathrm{T}=\begin{cases} K\delta & , \quad for\ \delta_m \le \delta_m^0 \\ (1-d)K\delta & , \quad for\ \delta_0 \le \delta_m \le \delta_m^f \\ 0 & , \quad for\ \delta_m \ge \delta_m^f \end{cases} \tag{3}$$

where δ_m is the effective displacement, which represents the combination of normal and shear deformations. K is the initial penalty stiffness, expressed as follows:

$$\delta_m=\sqrt{\langle \max(\delta_n,0)\rangle^2+\delta_s^2+\delta_s^2}\,d=\frac{\delta_m^f\left(\delta_m-\delta_m^0\right)}{\delta_m\left(\delta_m^f-\delta_m^0\right)} \tag{4}$$

The effective displacements corresponding to damage initiation and complete failure under mixed-mode loading are denoted as δ_m^0 and δ_m^f, respectively. These displacements are determined using Equations (1) and (2), respectively. Notably, during normal compressive loading, the normal stress remains unaffected by damage [16].

3.2.2. Finite Element Modeling

The multilayer shell modeling approach was employed in ABAQUS to investigate the delamination-driven buckling of the fabricated sandblasted and polished metal–composite cylinders. Zhang et al. [66] applied this approach to predict the buckling behavior of composite-repaired cylinders. A finite element model (Figure 13) of the sandblasted and polished metal–composite cylinders was created, using the commercial preprocessing software HyperMesh version 14.0. In Figure 13a, the yellow shell represents the actual geometric shape obtained through 3D scanning, which was meshed using four-node quadrilateral elements (S4 elements). On the basis of the S4 mesh, 3D meshes were generated for the inner steel layer (red), middle resin layer (yellow), and outer composite layer (green) of the metal–composite cylinders. These layers were meshed using the same approach, ensuring that the nodes on the interfaces between the layers had the same geometric coordinates. The mesh types for the steel, resin, and composite layers were C3D8R, COH3D8, and SC8R, respectively. A mesh convergence study revealed that a mesh size of 2.5 mm resulted in the highest computational efficiency (Figure 14). The finite element data for the four fabricated cylinders are presented in Table 6.

Linear eigenvalue and nonlinear Riks analyses were conducted to investigate the delamination buckling of the four fabricated cylinders. As displayed in Figure 13b, three nodes in each finite element model were constrained to prevent rigid-body displacement and enable controlled deformation under load. The China Classification Society recommends this boundary condition for the analyzing the buckling characteristics in shells of revolution [67]. This boundary condition has been effectively utilized in studies investigating the buckling characteristics of different cylindrical shells [7–9,68,69]. The first eigenmode is typically a good estimate of the worst shape. This method of analysis is recommended under Chinese regulations [67]. In nonlinear Riks analysis on ABAQUS, the cohesive zone model often exhibits convergence difficulties when it simulates stiffness

degradation. To address this problem, a viscous regularization method was applied to the constitutive equations of this model. A viscosity parameter of 1.75 was specified in the stiffness equations, to improve convergence [70].

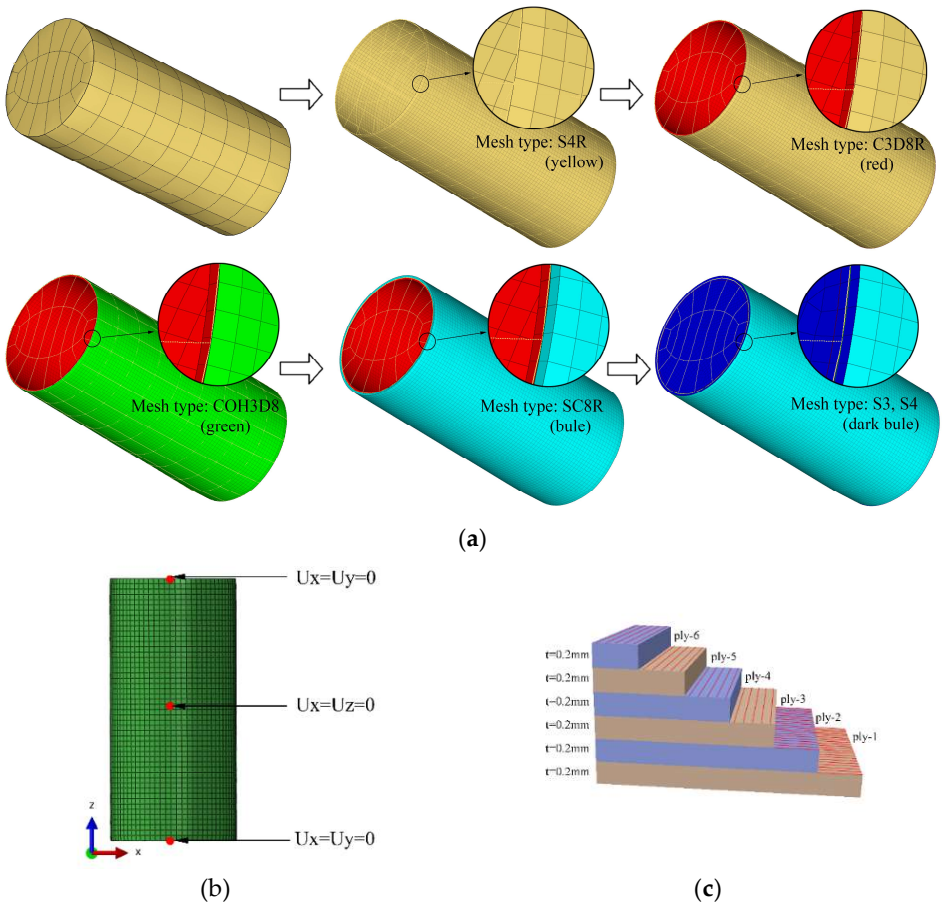


Figure 13. Finite element models of sandblasted and polished metal–composite cylinders: (**a**) modeling process, (**b**) constraint conditions, and (**c**) wrapping angle.

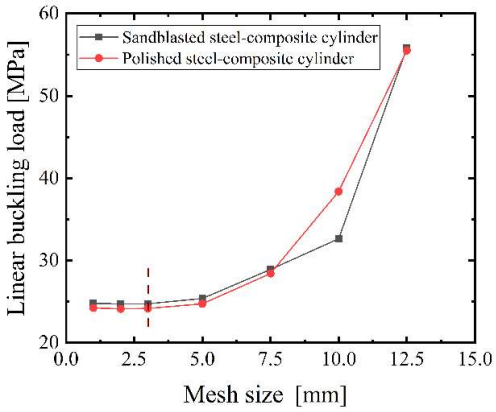


Figure 14. Results of convergence study for representative sandblasted and polished metal–composite cylinders.

The mechanical characteristics of T300 composites and the cohesive zone [63,71] are presented in Table 7. The composite layer was wrapped in the sequence of $[0_3/90_4]$, where the 0° reference direction was aligned with the axial direction of the cylinder (Figure 13c). The tensile strength of cohesive interfaces was considerably influenced by the surface treatment method [72], with polished surfaces exhibiting relatively low interlaminar tensile

strength because of insufficient mechanical interlocking. The properties of the steel cylinder of the fabricated specimens were as follows: Young's modulus (E) = 200 GPa, Poisson's μ = 0.291, and yield strength (σ_y) = 628 MPa. In this study, the Hashin criterion and quadratic nominal stress criterion were used to evaluate the failure of the composite and adhesive.

Table 6. Finite element data for sandblasted and polished metal–composite cylinders and corresponding numerical analysis results.

Sample	S4R	S3	COH3D8	C3D8R	SC8R	P_{linear} [MPa]	P_{non} [MPa]	P_{non}/P_{test}
Sandblasted cylinder-1	2887	14	8175	8175	8175	24.1	22.2	1.012
Sandblasted cylinder-2	3225	34	8175	8175	8175	26.0	23.4	1.051
Polished cylinder-1	2632	92	8175	8175	8175	26.6	15.8	1.023
Polished cylinder-2	3038	106	8175	8175	8175	24.7	14.3	1.094

Note: S4R is 4-node doubly curved shell element with reduced integration; S3 is 3-node shell element; COH3D8 is 8-node 3D cohesive element; C3D8R is 8-node linear brick element with reduced integration; SC8R is 8-node continuum shell element with reduced integration.

Table 7. The mechanical characteristics of T300 composites and the cohesive region.

Parameter		Value	Parameter		Value (Sandblast)	Value (Polish)
Elastic modulus (GPa)	E_1	138	Critical strain energy release rate (N/mm)	G_{IC}	0.0876	0.0876
	E_2	10.16		G_{IIC}	0.3152	0.3152
	E_3	10.16		G_{IIIC}	0.3152	0.3152
Poisson's ratio	v_{12}	0.28	Interlaminar tensile strength (MPa)	σ_n^0	44.54	0.6
	v_{13}	0.28		τ_{13}^0	106.9	1.4
	v_{23}	0.3		τ_{23}^0	106.9	1.4
Shear modulus (GPa)	G_{12}	5.86	Penalty stiffness (N/mm^3)	K_n^0	10^6	10^6
	G_{12}	5.86		K_{13}^0	10^6	10^6
	G_{23}	4.79		K_{23}^0	10^6	10^6
			Viscosity	η	1.75	1.75

3.2.3. Numerical Results and Discussion

The linear eigenvalue modes of the fabricated sandblasted and polished metal–composite cylinders were similar, containing axial half-waves and four circumferential waves (Figure 15). The sandblasted and polished metal–composite cylinders had average linear eigenvalues of 25.65 and 25.05 MPa, respectively; thus, the polished cylinders had a 2.3% lower average linear eigenvalue than did the sandblasted cylinders. These results indicate that linear eigenvalue analysis could not predict the intralaminar progressive failure of the resin layer. Such analysis is based on linear elasticity theory, so does not account for material damage or geometric nonlinear deformation before buckling. Therefore, nonlinear Riks analysis was performed to further examine the delamination buckling of the aforementioned cylinders under progressive damage conditions.

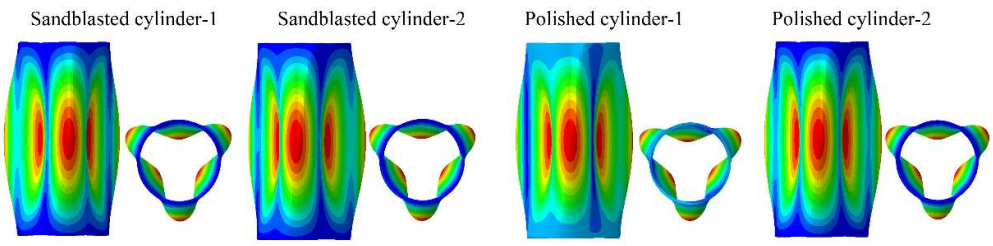


Figure 15. Linear eigenvalue modes of sandblasted and polished metal–composite cylinders.

The results of the nonlinear Riks analysis indicated that surface treatment of the metal liner considerably increased the load-bearing capacity of the metal–composite cylinders. The numerical and experimental collapse pressures for the fabricated metal–composite cylinders are listed in Table 6. The average nonlinear buckling load of the fabricated sandblasted metal–composite cylinders (22.8 MPa) was 51.5% higher than that of the fabricated polished metal–composite cylinders (15.05 MPa), highlighting the critical role of surface treatment in enhancing the manufacturing quality and performance of metal–composite cylinders. The ratio of the numerical nonlinear buckling load to the experimental collapse pressure ranged from 1.012 to 1.094. This result indicates that the multilayer shell model based on cohesive elements accurately predicted the buckling load under progressive damage conditions. The large deviation (9.4%) observed for polished metal–composite cylinder 2 was attributable to the idealized geometric model, which was based on the assumption that the cylinder material was homogeneous and perfect. Potential manufacturing imperfections such as uneven thickness distribution, resin-rich regions, composite wrinkling, and voids in resin were not considered in the numerical analysis.

An appropriate surface treatment method can enable the effective control of the delamination buckling characteristics of metal–composite cylinders. The equivalent paths of the four fabricated cylinders exhibited unstable buckling characteristics. As displayed in Figure 16, during the initial stage, the displacement of the collapse point of the cylinders increased linearly with the load acting on them. At this stage, the equivalent path curves of the sandblasted and polished metal–composite cylinders were nearly identical, which was attributable to their similar stiffness. However, after the onset of delamination (from P_{pc2} to P_{pc3}), the polished cylinders exhibited a slightly lower stiffness than did the sandblasted cylinders, leading to the earlier buckling of the polished cylinders. As structural stiffness further decreased and localized deformation or instability developed, a nonlinear stage emerged near the collapse point. Finally, the equivalent path of the sandblasted cylinders exhibited a sharp downward trend, displaying highly unstable buckling characteristics (from P_{sc4} to P_{sc3}) immediately after the onset of delamination. In contrast to the sandblasted cylinders, the polished cylinders exhibited a progressive reduction in stiffness with delamination propagation, resulting in them showing a steeper downward trend in the equivalent path compared with that shown by the sandblasted cylinders.

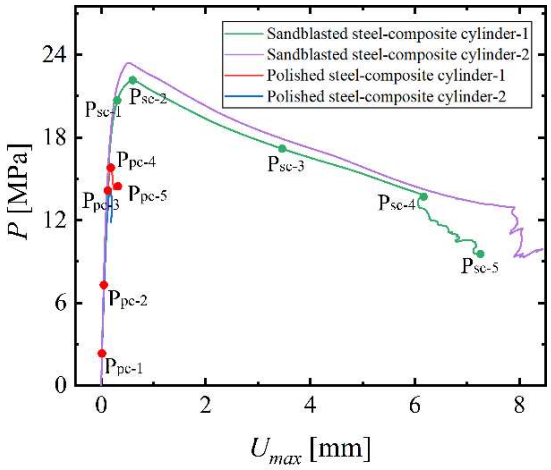


Figure 16. Pressure-displacement curves for sandblasted and polished metal–composite cylinders.

The delamination buckling mechanisms of the sandblasted and polished metal–composite cylinders exhibited notable differences, due to the distinct treatment processes applied to the cylinders. The failure modes of the sandblasted and polished metal–composite cylinders involved the formation of local concavities (Figure 11), which was consistent with

the experimental results (in Section 3.1.3). These failure modes were also consistent with the observations during the delamination of composite and metal–composite cylinders [25,44]. The representative deformation and delamination evolution processes of the sandblasted and polished metal–composite cylinders are displayed in Figures 16–20, respectively. The failure behavior of the sandblasted and polished cylinders differed significantly in terms of delamination initiation and buckling progression. For the sandblasted cylinders, after the critical buckling load (Psc-2) was reached, the stiffness of the adhesive layer in the middle region began to degrade. This degradation led to delamination at the end of the post-buckling stage, suggesting that large deformations primarily drove delamination in the sandblasted cylinders. In contrast, the polished cylinders exhibited a different buckling behavior. Due to the weaker bond strength resulting from the polishing treatment, these cylinders experienced delamination prior to reaching the critical buckling load (Ppc-4). This earlier initiation of delamination in the polished cylinders was accompanied by substantial resin-layer delamination, aligning with the experimental observations (Section 3.1.3). The early delamination in the polished cylinders significantly affected their structural stability, leading to a lower buckling load compared to the sandblasted cylinders. In addition, the resin layer of these cylinders experienced considerable delamination, which was consistent with the experimental results (in Section 3.1.3). Delamination propagation had a stress-relaxing effect on the polished cylinders [73], resulting in their buckling load being substantially lower than that of the sandblasted cylinders.

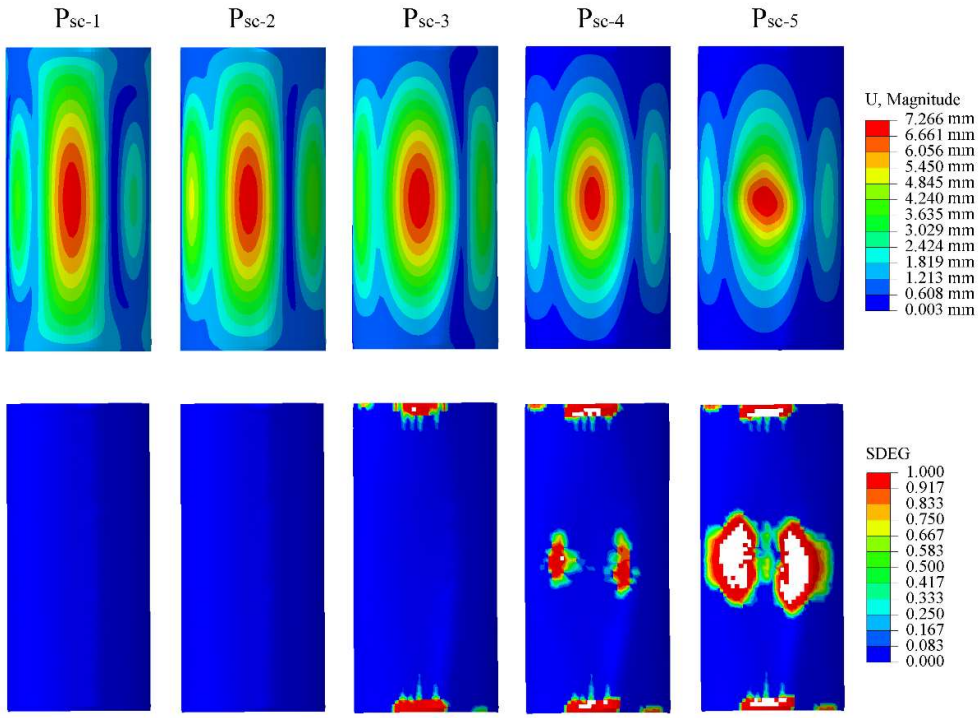
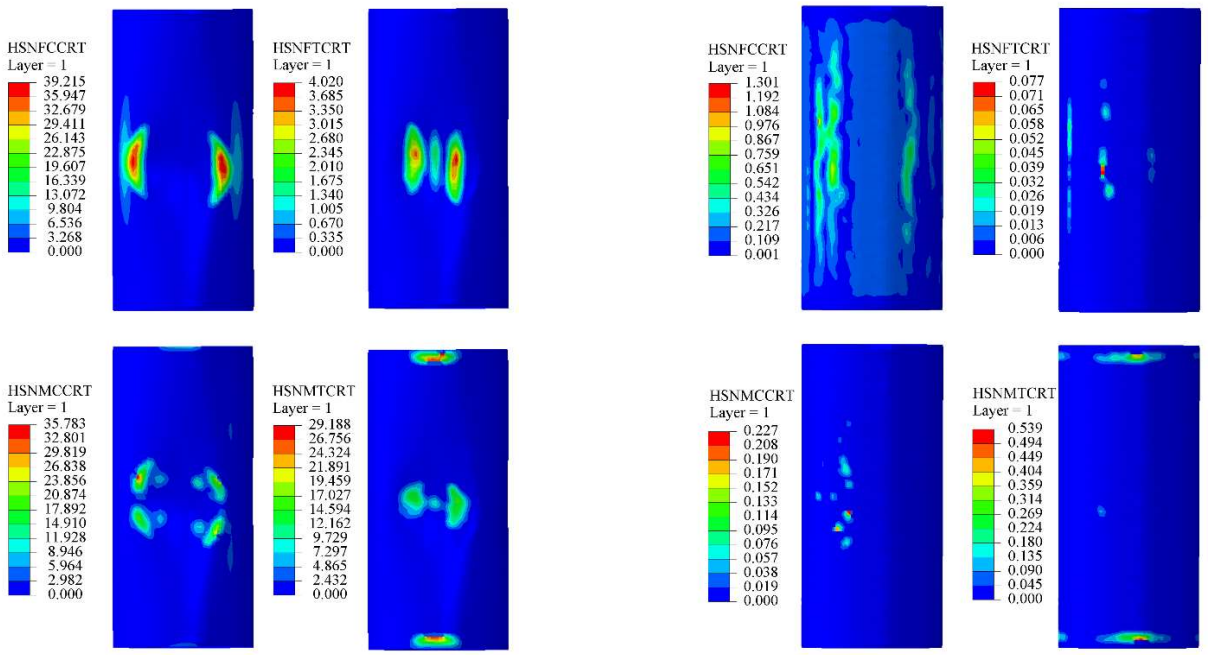


Figure 17. Evolution of deformation and delamination (SDEG is dimensionless quantities) in sandblasted metal–composite cylinder 1 for the five points in Figure 16 ($P_{sc\text{-}2}$ corresponds to the critical buckling load).



(**a**) (**b**)

Figure 18. Hashin's damage (dimensionless quantities) for sandblasted metal–composite cylinder 1 during the (**a**) critical-buckling and (**b**) post-buckling stages.

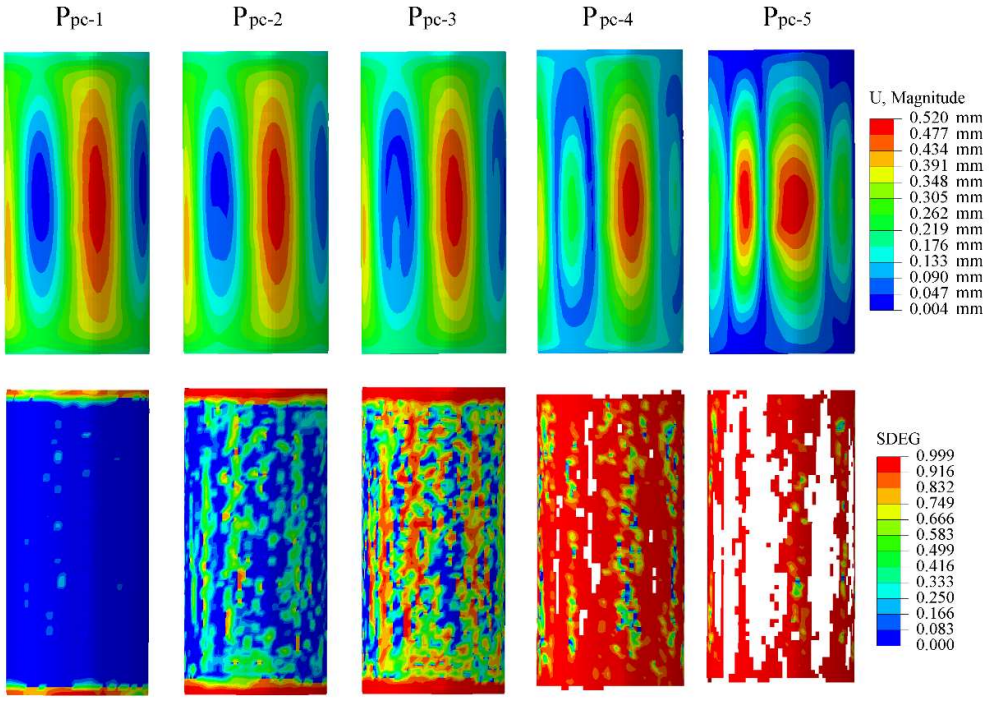


Figure 19. Evolution of deformation and delamination (SDEG is dimensionless quantities) in polished metal–composite cylinder 1 for the five points in Figure 16 (P_{pc-4} corresponds to the critical buckling load).

The failure of the composite layers of the sandblasted and polished metal–composite cylinders was analyzed by the Hashin criterion. Figures 16–20 depict the representative damage statuses of the composite layers in the sandblasted metal–composite cylinder 1 and polished metal–composite cylinder 1, respectively, during the critical buckling and post-buckling stages. At the critical buckling load, the fiber failure initiation criterion (compression: HSNFCCRT, traction: HSNFTCRT) and matrix failure initiation criterion

(compression: HSNFTCRT, tension: HSNFTCRT) of the sandblasted cylinders were less than 1 (Figure 18a). This result indicates that the sandblasted cylinders had mechanical integrity in the critical buckling stage. The post-buckling failure criteria of these cylinders exceeded 1, indicating the failure of the composite layer. This result is consistent with the experimental observations mentioned in Section 3.1.3. Premature resin failure reduced the values of the failure initiation criteria (Figure 20) in the critical buckling stage of the polished cylinders. This result was attributable to the polishing treatment, which reduced the bond strength and structural integrity of these cylinders. In the experimental analysis, both the fiber and resin of the polished cylinders failed completely, which differed from the fiber compression failure observed in the numerical analysis. Slightly complex failure modes and an increased failure area in the experimental results have been observed in many tests of composite mechanical properties [74–77]. These phenomena might be caused by the introduction of defects during the use of manual layup and vacuum bagging techniques.

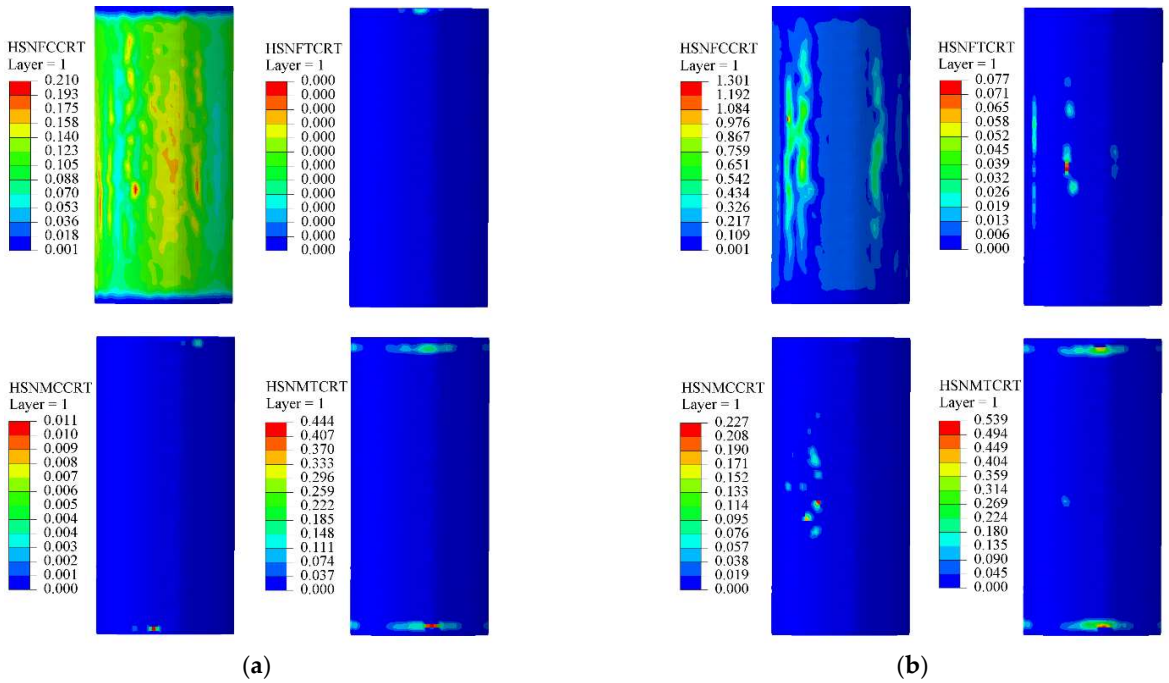


Figure 20. Hashin's damage (dimensionless quantities) for polished metal–composite cylinder 1 during the (**a**) critical-buckling and (**b**) post-buckling stages.

3.3. Effects of Cohesive Zone Parameters and Geometric Imperfection on the Buckling Load

To explore the effects of cohesive zone parameters on the buckling load of metal–composite cylinders with different thickness-to-diameter (t/D) ratios, numerical models with t/D ratios of 0.033, 0.023, and 0.016 were constructed. The buckling load was analyzed under attenuation ratios of 0%, 60%, 80%, 90%, 94%, 97%, and 99% for the critical strain-energy release rate, interlaminar tensile strength, and penalty stiffness. The first-order eigenmode was considered to be an initial imperfection, with an amplitude of 0.1t. The geometric dimensions of the considered metal–composite cylinder were consistent with the nominal dimensions listed in Table 3. Moreover, the modeling approach and analysis procedures were consistent with those described in Section 3.2.2. Since the cohesive zone model and geometric imperfections have no impact on the collapse mode, which consistently exhibits typical local concavities, they are not discussed in this section.

Among the three examined cohesive zone parameters, the interlaminar tensile strength had the strongest influence on the buckling load of the considered metal–composite cylinder. As shown in Figure 21a–c, the buckling load was almost unaffected by the strain-energy

release rate and penalty stiffness, because interlaminar tensile strength directly determines the failure strength of the interface under tensile loading. In contrast, the strain-energy release rate and penalty stiffness primarily influence the propagation and stability of interface damage. These two factors have a minimal influence on the buckling load, because buckling is primarily governed by the global structural stability and geometric imperfections, rather than local interface damage. A slight reduction in buckling load was observed when the attenuation ratio of interlaminar tensile strength reached 99%. This result was attributable to the excessively low penalty stiffness, which artificially reduced the structural stiffness and might have led to inaccurate predictions [78]. The black dashed lines in Figure 21 represents the buckling load of the fully delaminated metal–composite cylinder, which was obtained through numerical analysis based on GAP elements (i.e., the GAP method employed by Zhang et al. [44]). When t/D was 0.033 and the attenuation ratio of the interlaminar tensile strength was 99%, the cohesive zone model and GAP element method produced similar buckling loads. However, as the t/D value decreased, the difference in the buckling loads obtained with these methods progressively increased. The results indicate that for t/D values smaller than 0.016, an adhesive with high tensile strength should be used to reduce the potential for delamination.

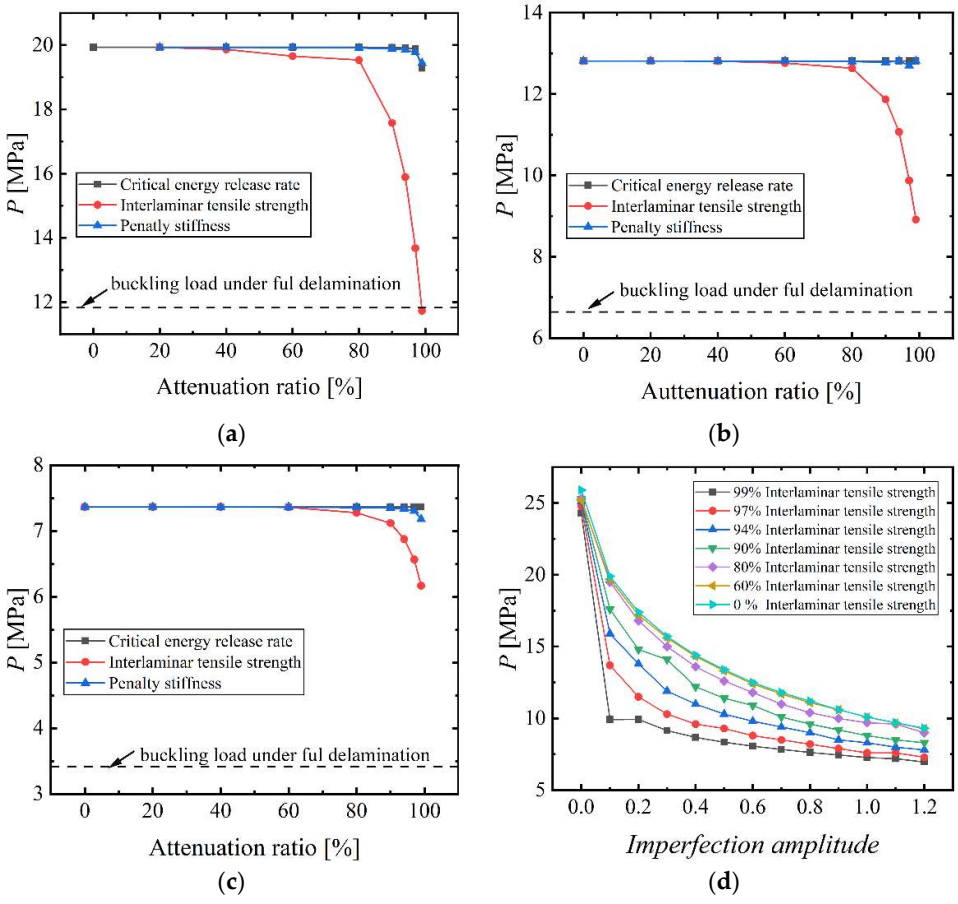


Figure 21. Nonlinear buckling load of the considered metal–composite cylinder under different geometric, cohesion, and imperfection parameters: (**a**) thickness-to-diameter ratio (t/D) = 0.033, (**b**) t/D = 0.023, (**c**) t/D = 0.0157, and (**d**) t/D = 0.033.

Metal–composite cylinders are imperfection-sensitive structures [7–9]; thus, exploring the influences of cohesive zone parameters on imperfection sensitivity is essential. Seven representative interlaminar tensile strengths were selected to examine these influences. As depicted in Figure 21d, the buckling load exhibited a consistent monotonic decrease as

the attenuation ratio of the interlaminar tensile strength was increased from 0% to 80%. This result suggests that enhancing interlaminar tensile strength through surface treatment techniques (e.g., sandblasting, laser processing, and anodization) has a negligible influence on the imperfection sensitivity of metal–composite cylinders. At small imperfection amplitudes (0–0.1t), the imperfection sensitivity of the examined metal–composite cylinder increased with the attenuation ratio of the interlaminar tensile strength, reaching its maximum level when this ratio was 99%. As the imperfection amplitude was increased from 0.1t to 1.2t, the imperfection sensitivity of the metal–composite cylinder reduced. This result suggests that when the interlaminar tensile strength of a metal–composite cylinder is low, its geometric imperfections must be minimized, to reduce the potentially catastrophic effects of delamination and geometric imperfections on the load-bearing capacity.

4. Conclusions

This study investigated the mechanical properties of adhesively bonded steel specimens and the delamination buckling characteristics of metal–composite cylinders with different interfacial strengths, through both numerical and experimental methods. Additionally, the enhancement mechanisms were clarified through detailed characterization and mechanical testing. The main conclusions of this study are as follows:

(1) The bond strength of sandblasted specimens was significantly higher than that of polished specimens in single-lap shear tests. The specimen subjected to 80-mesh sandblasting treatment exhibited a 256% higher bond strength than did the polished specimens. The improvement in bond strength was attributable to the increased surface quality produced through sandblasting, which enlarged the effective bonding area and promoted stronger mechanical interlocking.

(2) The collapse modes of both sandblasted and polished metal–composite cylinders exhibited local concavities. The average collapse pressure of the fabricated sandblasted cylinders was 22.011 MPa, which was 55.0% higher than that of the polished cylinders (14.851 MPa). Moreover, the delamination area of the polished cylinders was substantially larger than that of the sandblasted cylinders because of the improved adhesion between the metal and composite layers in the polished cylinders.

(3) An appropriate surface treatment method can effectively control the delamination buckling characteristics of metal–composite cylinders. In the pre-buckling stage, polishing treatment causes a slight reduction in stiffness because of the onset of delamination. In the post-buckling stage, the equilibrium path curve of sandblasted metal–composite cylinders initially exhibits a sharp downward trend, with unstable buckling characteristics emerging after delamination. Polished metal–composite cylinders exhibit a steeper downward trend in the equilibrium path than do sandblasted metal–composite cylinders, because of the propagation of delamination in the polished cylinders.

(4) Among various cohesive zone parameters, the interlaminar tensile strength of the adhesive has the strongest effect on the buckling load of metal–composite cylinders. For thickness-to-diameter (t/D) ratios smaller than 0.016, an adhesive with high tensile strength should be used to reduce the potential of delamination. Metal–composite cylinders with low interlaminar tensile strength exhibit high sensitivity to small imperfections (imperfection amplitudes ranging from 0 to 0.1t.); thus, minimizing the geometric imperfections of these cylinders is essential for ensuring that their buckling load is sufficient.

These findings provide critical guidance for the design and manufacturing of deep-sea pressure hulls and other marine structures, enabling the industry to optimize material selection and fabrication processes to improve structural reliability and performance in extreme underwater environments. Future research should investigate the influences of bonding parameters on the buckling characteristics of composite cylinders by the Virtual Crack

Closure Technique (VCCT). It should also focus on the long-term durability of sandblasted interfaces in marine environments, explore hybrid surface treatments to improve bonding performance, and study the impact of dynamic loading on delamination and buckling. These efforts, combined with numerical modeling and experimental validation, will help better understand and improve the structural performance of composite cylinders under complex conditions.

Author Contributions: C.D.: methodology, software, data curation, writing—original draft. Y.H.: validation, resources, writing—review and editing, visualization. H.J.: validation, writing—review and editing. S.K.: investigation, validation, writing—review and editing. J.Z.: conceptualization, methodology, resources, writing—review and editing, project administration, funding acquisition. All authors have read and agreed to the published version of the manuscript.

Funding: This study was supported by the National Natural Science Foundation of China (grant number: 52471285 and 52405368) and the Science Fund for Distinguished Young Scholars of Jiangsu Province (grant number: BK20230014).

Data Availability Statement: The raw data supporting the conclusions of this article will be made available by the authors on request.

Conflicts of Interest: The authors declare no conflict of interest.

References

1. Cui, W.; Lian, L.; Pan, G. Frontiers in deep-sea equipment and technology. *J. Mar. Sci. Eng.* **2023**, *11*, 715. [CrossRef]
2. Zhang, J.; Wang, X.; Tang, W.; Wang, F.; Zhu, Y. Non-linear collapse behavior of externally pressurized resin toroidal and cylindrical shells: Numerical and experimental studies. *Ships Offshore Struct.* **2021**, *16*, 529–545. [CrossRef]
3. Sheta, A.; Ma, X.; Zhuge, Y.; ElGawady, M.; Mills, J.E.; Abd-Elaal, E. Axial compressive behaviour of thin-walled composite columns comprise high-strength cold-formed steel and PE-ECC. *Thin-Walled Struct.* **2023**, *184*, 110471. [CrossRef]
4. Hosseini, S.M.; Shariati, M. Experimental analysis of energy absorption capability of thin-walled composite cylindrical shells by quasi-static axial crushing test. *Thin-Walled Struct.* **2018**, *125*, 259–268. [CrossRef]
5. Xie, L.; Qi, Y.; Bai, Y.; Qiu, C.; Wang, H.; Fang, H.; Zhao, X. Sandwich assemblies of composites square hollow sections and thin-walled panels in compression. *Thin-Walled Struct.* **2019**, *145*, 106412.
6. Hu, Y.; Wei, Y.; Han, G.; Zhang, J.; Sun, G.; Hu, X.; Cheng, F. Comparison of impact resistance of carbon fibre composites with multiple ultra-thin CNT, aramid pulp, PBO and graphene interlayers. *Compos. Part A Appl. Sci. Manuf.* **2022**, *155*, 106815. [CrossRef]
7. Zuo, X.; Zhang, J.; Tang, W.; Li, Y.; Li, H. Buckling behavior of steel and steel–composite cylinders under external pressure. *Thin-Walled Struct.* **2022**, *181*, 110011. [CrossRef]
8. Zuo, X.; Zhang, J.; Tang, W.; Li, Y.; Zhan, M. Collapse of externally pressurized elliptical steel cylinders stiffened with helical composite stripes. *Ocean Eng.* **2022**, *263*, 112376. [CrossRef]
9. Zuo, X.; Tang, W.; Zhang, J.; Li, Y.; Zhan, M. Collapse of externally pressurized steel–composite hybrid cylinders: Analytical solution and experimental verification. *Metals* **2022**, *12*, 1591. [CrossRef]
10. Hilburger, M.W.; Starnes, J.H. Effects of imperfections of the buckling response of composite shells. *Thin-Walled Struct.* **2004**, *42*, 369–397. [CrossRef]
11. Fazlalipour, N.; Showkati, H. Geometric properties and imperfections influence on buckling behavior of Variable-Thickness steel cylindrical shells subjected to combined Loading: Experimental and numerical study. *Structures* **2023**, *55*, 834–852. [CrossRef]
12. Tsouvalis, N.G.; Zafeiratou, A.A.; Papazoglou, V.J. The effect of geometric imperfections on the buckling behaviour of composite laminated cylinders under external hydrostatic pressure. *Compos. B Eng.* **2003**, *34*, 217–226. [CrossRef]
13. Hartwich, T.S.; Panek, S.; Wilckens, D.; Wille, T.; Krause, D. The influence of R/t-ratio on the imperfection sensitivity of the buckling load of thin-walled CFRP cylindrical shells. *Compos. Struct.* **2024**, *341*, 118216. [CrossRef]
14. Wang, W.; Zhu, Y.; Zhou, L.; Zhang, J. Buckling characteristics of carbon fiber composite/aluminium alloy combined cylindrical shells under external hydrostatic pressure. *Int. J. Press. Vessel. Pip.* **2024**, *208*, 105125. [CrossRef]
15. Cai, B.; Liu, Y.; Liu, Z.; Tian, X.; Ji, R.; Li, H. Reliability-based load and resistance factor design of composite pressure vessel under external hydrostatic pressure. *Compos. Struct.* **2011**, *93*, 2844–2852. [CrossRef]
16. Li, B.; Pang, Y.; Cheng, Y.; Zhu, X. Collaborative optimization for ring-stiffened composite pressure hull of underwater vehicle based on lamination parameters. *Int. J. Nav. Archit. Ocean Eng.* **2017**, *9*, 373–381. [CrossRef]

17. Sumana, B.G.; Vidya Sagar, H.N.; Sharma, K.V.; Krishna, M. Numerical analysis of the effect of fiber orientation on hydrostatic buckling behavior of fiber metal composite cylinder. *J. Reinf. Plast. Compos.* **2015**, *34*, 1422–1432. [CrossRef]
18. Rezaiee-Pajand, M.; Arabi, E.; Masoodi, A.R. Nonlinear analysis of FG-sandwich plates and shells. *Aerosp. Sci. Technol.* **2019**, *87*, 178–189. [CrossRef]
19. Ghandehari, M.A.; Masoodi, A.R.; Hosseininia, E.S. Temperature-dependency and boundary condition impacts on the multiscale vibrational behavior of laminated nested dual conical shell structure semi-AUV applications. *Appl. Ocean Res.* **2025**, *154*, 104425. [CrossRef]
20. Zhang, L.; Zhao, L.; Pan, L.; Gao, J. Research progress of composite cylindrical shells. *Polym. Compos.* **2023**, *44*, 7298–7316. [CrossRef]
21. Kachanov, L.M. Layering in glass-fiber pipes subject to external pressure. *Polym. Mech.* **1976**, *11*, 947–949. [CrossRef]
22. Kachanov, L.M. Separation failure of composite materials. *Polym. Mech.* **1976**, *12*, 812–815. [CrossRef]
23. Rasheed, H.A.; Tassoulas, J.L. Delamination growth in long composite tubes under external pressure. *Int. J. Fract.* **2001**, *108*, 1–23. [CrossRef]
24. Fu, Y.; Yang, J. Delamination growth for composite laminated cylindrical shells under external pressure. *Appl. Math. Mech.* **2007**, *28*, 1131–1144. [CrossRef]
25. Wei, R.; Shen, K.; Pan, G. A numerical study on the effect of delamination on composite cylindrical shells subjected to hydrostatic pressure. *Ocean Eng.* **2022**, *262*, 112294. [CrossRef]
26. Qu, Y.; Chen, N.; Yuan, L. Cohesive zone model based reliability analysis for a sandwich pipe. *Ocean Eng.* **2023**, *270*, 113550. [CrossRef]
27. Wan, F.; Guan, F.; Zhou, C.; Liu, S.; Yang, T. Pressure capacity of sandwich pipe with cement-based core configuration under deep-water external pressure. *J. Sandw. Struct. Mater.* **2020**, *22*, 1292–1326. [CrossRef]
28. Yang, Y.; Wan, F.; Guan, F.; Tian, H.; Chen, W. Buckling behavior of sandwich pipe under external pressure and lateral load. *Int. J. Press. Vessel. Pip.* **2024**, *207*, 105114. [CrossRef]
29. Xie, P.; Lin, G.; Teng, J.G.; Jiang, T. Modelling of concrete-filled filament-wound FRP confining tubes considering nonlinear biaxial tube behavior. *Eng. Struct.* **2020**, *218*, 110762. [CrossRef]
30. Teng, J.; Fernando, D.; Yu, T.; Zhao, X. Debonding failures in CFRP-strengthened steel structures. In Proceedings of the 3rd Asia-Pacific Conference on FRP in Structures, Sapporo, Japan, 2–4 February 2012.
31. Teng, J.G.; Fernando, D.; Yu, T. Finite element modelling of debonding failures in steel beams flexurally strengthened with CFRP laminates. *Eng. Struct.* **2015**, *86*, 213–224. [CrossRef]
32. Fernando, D.; Teng, J.; Yu, T.; Zhao, X. Preparation and characterization of steel surfaces for adhesive bonding. *J. Compos. Constr.* **2013**, *17*, 04013012. [CrossRef]
33. Budhe, S.; Ghumatkar, A.; Birajdar, N.; Banea, M.D. Effect of surface roughness using different adherend materials on the adhesive bond strength. *Appl. Adhes. Sci.* **2015**, *3*, 20. [CrossRef]
34. Zielecki, W.; Pawlus, P.; Perłowski, R.; Dzierwa, A. Surface topography effect on strength of lap adhesive joints after mechanical pre-treatment. *Arch. Civ. Mech. Eng.* **2013**, *13*, 175–185. [CrossRef]
35. Kadlečková, M.; Minařík, A.; Smolka, P.; Mráček, A.; Wrzecionko, E.; Novák, L.; Musilová, L.; Gajdošík, R. Preparation of textured surfaces on aluminum-alloy substrates. *Materials* **2018**, *12*, 109. [CrossRef] [PubMed]
36. Ye, J.; Wang, H.; Dong, J.; Liu, C.; Gao, Y.; Gong, B.; Su, B.; Peng, H. Metal surface nanopatterning for enhanced interfacial adhesion in fiber metal laminates. *Compos. Sci. Technol.* **2021**, *205*, 108651. [CrossRef]
37. Maressa, P.; Anodio, L.; Bernasconi, A.; Demir, A.G.; Previtali, B. Effect of surface texture on the adhesion performance of laser treated Ti6Al4V alloy. *J. Adhes.* **2015**, *91*, 518–537. [CrossRef]
38. Schweizer, M.; Meinhard, D.; Ruck, S.; Riegel, H.; Knoblauch, V. Adhesive bonding of CFRP: A comparison of different surface pre-treatment strategies and their effect on the bonding shear strength. *J. Adhes. Sci. Technol.* **2017**, *31*, 2581–2591. [CrossRef]
39. Saleema, N.; Gallant, D. Atmospheric pressure plasma oxidation of AA6061-T6 aluminum alloy surface for strong and durable adhesive bonding applications. *Appl. Surf. Sci.* **2013**, *282*, 98–104. [CrossRef]
40. Wang, B.; Bai, Y.; Hu, X.; Lu, P. Enhanced epoxy adhesion between steel plates by surface treatmentand CNT/short-fibre reinforcement. *Compos. Sci. Technol.* **2016**, *127*, 149–157. [CrossRef]
41. Hu, Y.; Zhang, J.; Wang, L.; Jiang, H.; Cheng, F.; Hu, X. A simple and effective resin pre-coating treatment on grinded, acid pickled and anodised substrates for stronger adhesive bonding between Ti-6Al-4V titanium alloy and CFRP. *Surf. Coat. Technol.* **2022**, *432*, 128072. [CrossRef]
42. Hu, Y.; Yuan, B.; Cheng, F.; Hu, X. NaOH etching and resin pre-coating treatments for stronger adhesive bonding between CFRP and aluminium alloy. *Compos. B Eng.* **2019**, *178*, 107478. [CrossRef]
43. Choqueuse, D.; Bigourdan, B.; Deuff, A.; Douchin, B.; Quetel, L. Hydrostatic compression behaviour of steel composite hybrid tubes. In Proceedings of the ICCM17, Edinburgh, UK, 27–31 July 2009.

44. Di, C.; Zhang, J.; Hu, Y.; Kang, C. Buckling of steel-composite cylindrical pressure hulls with initial delamination. *Thin-Walled Struct.* **2024**, *202*, 112042. [CrossRef]
45. *ISO 25178-2:2021*; Geometrical Product Specifications (GPS)—Surface Texture: Areal—Part 2: Terms, Definitions and Surface Texture Parameters. IOS: Geneva, Switzerland, 2021.
46. *ASTM D5868*; Standard Test Method for Lap Shear Adhesion for Fiber Reinforced Plastic (FRP) Bonding. ASTM: West Conshohocken, PA, USA, 2014.
47. Mao, Y.; Dong, G.; Fu, Y.; Li, Y.; Huang, P.; Fu, S. High performance shape-adjustable structural lithium-ion battery based on hybrid fiber reinforced epoxy composite. *Compos. Struct.* **2023**, *325*, 117598. [CrossRef]
48. Esmaeili, Y.R.; Cosco, B.; Najjaran, H. Vacuum bag leak detection for resin infusion: An electric current–based analogy. *Int. J. Adv. Manuf. Technol.* **2023**, *124*, 1775–1786. [CrossRef]
49. Hu, C.; Xu, Z.; Huang, M.; Cai, C.; Wang, R.; He, X. An insight into the mechanical behavior and failure mechanisms of T-stiffened composite structures with through-interface debonding defects. *Ocean Eng.* **2024**, *300*, 117342. [CrossRef]
50. *ISO 16809:2017*; International Organisation for Standardisation, Non-Destructive Testing—Ultrasonic Thickness Measurement. IOS: Geneva, Switzerland, 2017.
51. Wang, J.; Ai, C.; Yun, X.; Chen, Z.; He, B. Effects of 3D roughness parameters of sandblasted surface on bond strength of HVOF sprayed WC-12Co coatings. *Coatings* **2022**, *12*, 1451. [CrossRef]
52. Zhang, C.; Zhang, Y.; Chen, L. Crater array generated on Al alloy surface by nanosecond laser: Surface characteristics and bonding strength. *Opt. Laser Technol.* **2024**, *169*, 110079. [CrossRef]
53. Ourahmoune, R.; Salvia, M.; Mathia, T.G.; Mesrati, N. Surface morphology and wettability of sandblasted PEEK and its composites: Surface morphology and wettability. *Scanning* **2014**, *36*, 64–75. [CrossRef]
54. Wenzel, R.N. Resistance of solid surfaces to wetting by water. *Ind. Eng. Chem.* **1936**, *28*, 988–994. [CrossRef]
55. Ebnesajjad, S.; Landrock, A.H. *Adhesives Technology Handbook*, 3rd ed.; William Andrew Publishing: New York, NY, USA, 2014.
56. Levy, A.; Hubert, P. Vacuum-bagged composite laminate forming processes: Predicting thickness deviation in complex shapes. *Compos. Part A Appl. Sci. Manuf.* **2019**, *126*, 105568. [CrossRef]
57. Wang, X.; Zhao, B.; Ding, W.; Pu, C.; Peng, S.; Ma, F. A short review on machining deformation control of aero-engine thin-walled casings. *Int. J. Adv. Manuf. Technol.* **2022**, *121*, 2971–2985. [CrossRef]
58. Zhang, J.; Teng, Y.; Di, C.; Zuo, X.; Wang, F. Collapse of composite-repaired cylinders with internal metal loss subjected to external hydrostatic pressure. *Mar. Struct.* **2023**, *88*, 103347. [CrossRef]
59. Zhang, J.; Liu, C.; Tang, W.; Wang, F.; Zhao, X.; Zhang, J.; Tang, L. Collapse of barreled frustums under external hydrostatic pressure. *Mar. Struct.* **2022**, *84*, 103218. [CrossRef]
60. Zhang, J.; Cheng, P.; Wang, F.; Tang, W.; Zhao, X. Hydroforming and buckling of an egg-shaped shell based on a petal-shaped preform. *Ocean Eng.* **2022**, *250*, 111057. [CrossRef]
61. Zhang, J.; Dai, M.; Wang, F.; Tang, W.; Zhao, X.; Zhu, Y. Theoretical and experimental study of the free hydroforming of egg-shaped shell. *Ships Offshore Struct.* **2022**, *17*, 257–267. [CrossRef]
62. Zhang, J.; Wang, F.; Wang, F.; Zhao, X.; Tang, W.; Chen, F. Buckling properties of bulged barrels under external pressure. *Thin-Walled Struct.* **2021**, *168*, 108226. [CrossRef]
63. Ameri, B.; Moradi, M.; Mohammadi, B.; Salimi-Majd, D. Investigation of nonlinear post-buckling delamination in curved laminated composite panels via cohesive zone model. *Thin-Walled Struct.* **2020**, *154*, 106797. [CrossRef]
64. Mohammadi, B.; Salimi-Majd, D. Investigation of delamination and damage due to free edge effects in composite laminates using cohesive interface elements. *Eng. Solid Mech.* **2014**, *2*, 101–118. [CrossRef]
65. Heidari, M.; Salimi-Majd, D.; Mohammadi, B. Failure analysis of composite wing adhesive joints using 3D cohesive interface element. *J. Compos. Sci. Technol.* **2015**, *2*, 31–40.
66. Zhang, Y.; Liu, Z.; Xin, J.; Wang, Y.; Zhang, C.; Zhang, Y. The attenuation mechanism of CFRP repaired corroded marine pipelines based on experiments and FEM. *Thin-Walled Struct.* **2021**, *169*, 108469. [CrossRef]
67. China Classification Society. *Rules For Classification of Diving Systems and Submersibles*; China Classification Society: Beijing, China, 2018.
68. Zhang, J.; Zhang, S.; Cui, W.; Zhao, X.; Tang, W.; Wang, F. Buckling of circumferentially corrugated cylindrical shells under uniform external pressure. *Ships Offshore Struct.* **2019**, *14*, 879–889. [CrossRef]
69. Zhang, J.; Zhu, Z.; Wang, F.; Zhao, X.; Zhu, Y. Buckling behaviour of double-layer and single-layer stainless steel cylinders under external pressure. *Thin-Walled Struct.* **2021**, *161*, 107485. [CrossRef]
70. Liu, P.; Gu, Z.; Hu, Z. Revisiting the numerical convergence of cohesive-zone models in simulating the delamination of composite adhesive joints by using the finite-element analysis. *Mech. Compos. Mater.* **2016**, *52*, 651–664. [CrossRef]
71. Zhang, J.; Wang, X.; Tang, W.; Wang, F.; Yin, B. Experimental and numerical buckling analysis of toroidal shell segments under uniform external pressure. *Thin-Walled Struct.* **2020**, *150*, 106689. [CrossRef]

72. Jiang, S.; Zhang, A.; Zhan, X.; Jiang, H. Surface microtexturing design, laser-etching and adhesive failure of aluminum alloy single-lap-joint: Experiment and simulation. *Thin-Walled Struct.* **2023**, *193*, 111237. [CrossRef]
73. Orifici, A.C.; de Zarate Alberdi, I.O.; Thomson, R.S.; Bayandor, J. Compression and post-buckling damage growth and collapse analysis of flat composite stiffened panels. *Compos. Sci. Technol.* **2008**, *68*, 3150–3160. [CrossRef]
74. Dogan, C.; Kaman, M.O.; Erdem, S.; Albayrak, M. Comparison of Hashin and Puck criterions for failure behavior of pin loaded composite plates. *Materwiss. Werksttech.* **2024**, *55*, 314–329. [CrossRef]
75. Rahman, M.M.; Ismail, A.E.; Ramli, M.F.; Abdul Rashid, A.H. A review of experimentation numerical simulation of low-velocity impact performances and damages of fiber-reinforced composites. *J. Adv. Res. Appl. Mech.* **2024**, *123*, 147–184. [CrossRef]
76. Al-Azzawi, A.S.M.; Featherston, C.A.; Lupton, C.; Jiang, C.; Barouni, A.; Koklu, U.; Giasin, K. Impact characteristics of S2-glass fibre/FM94-epoxy composites under high and cryogenic temperatures: Experimental and numerical investigation. *Compos. B Eng.* **2024**, *287*, 111786. [CrossRef]
77. Huang, Y.; Zhang, Y.; Kong, B.; Gu, J.; Wang, Z.; Chen, P. Experimental and numerical studies on buckling and post-buckling behavior of T-stiffened variable stiffness panels. *Chin. J. Aeronaut.* **2024**, *37*, 459–470. [CrossRef]
78. Lu, X.; Ridha, M.; Chen, B.Y.; Tan, V.B.C.; Tay, T.E. On cohesive element parameters and delamination modelling. *Eng. Fract. Mech.* **2019**, *206*, 278–296. [CrossRef]

Disclaimer/Publisher's Note: The statements, opinions and data contained in all publications are solely those of the individual author(s) and contributor(s) and not of MDPI and/or the editor(s). MDPI and/or the editor(s) disclaim responsibility for any injury to people or property resulting from any ideas, methods, instructions or products referred to in the content.